Department of Physics and Astronomy

University of Heidelberg

Diploma Thesis

in Physics

submitted by

Stefan Wagner

born in Memmingen

2010

Ionization Quenching by Low Energy Electrons
in the Double Chooz Scintillators

This diploma thesis has been carried out by Stefan Wagner

at the

Max-Planck-Institut für Kernphysik

under the supervision of

Prof. Dr. Manfred Lindner

Kurzfassung

Ziel des Double Chooz Experiments ist die Bestimmung von θ_{13} mit einer Sensitivität von $\sin^2 2\theta_{13} = 0.03$. Dazu wird im Experiment die Oszillation von Reaktor-$\bar{\nu}_e$ mit Hilfe zweier Flüssigszintillatordetektoren untersucht. Jeder der beiden Detektoren ist in vier Volumina aufgeteilt, die mit unterschiedlichen Flüssigkeiten gefüllt sind; drei davon mit verschiedenen Flüssigszintillatoren.

Diese Arbeit behandelt das Lichtausbeuteverhalten der Flüssigszintillatoren für niederenergetische Elektronen ($\lesssim 140$ keV). In diesem Energiebereich wird die Lichtausbeute aufgrund von Ionisationsquenching nichtlinear. Ein gutes Verständnis der Szintillator-Antwortfunktion ist wichtig für eine präzise Energierekonstruktion in der Analyse der Double Chooz Daten. Es wurde ein Compton-Koinzidenz-Experiment aufgebaut, um die Antwortfunktion der unterschiedlichen Flüssigszintillatoren im genannten Energiebereich zu studieren. Für die Analyse der Daten wurde eine spezielle Software entwickelt. Ein besonderes Augenmerk wurde auf die Kontrolle möglicher systematischer Fehler gelegt. Die Vorhersagen verschiedener Quenching-Modelle wurden auf Übereinstimmung mit den experimentellen Daten untersucht. Dabei wurde mit allen Modellen eine gute Übereinstimmung erzielt. Die Quenching-Parameter wurden für alle Modelle und Szintillatormischungen bestimmt.

Abstract

The Double Chooz experiment aims to measure θ_{13} with a sensitivity of $\sin^2 2\theta_{13} = 0.03$. For this purpose, the experiment investigates oscillations of $\bar{\nu}_e$ from nuclear reactors with two liquid scintillation detectors. Each detector is divided into four volumes, which are filled with four different liquids, three of them being different liquid scintillator mixtures.

This thesis deals with the light output of the liquid scintillators in response to low-energy electrons ($\lesssim 140$ keV). In this energy region the light yield is known to become non-linear due to ionization quenching. A firm knowledge of the light response function is important for an accurate energy reconstruction in the analysis of the Double Chooz data. A Compton coincidence experiment was set up to study the response function of the different Double Chooz liquid scintillators and a dedicated software was written for the analysis of the data. Special efforts were taken to control possible systematic errors. The predictions of various quenching models were tested for concordance with the data obtained. All of them were in good agreement with the experiment. The quenching parameters were obtained for each model and scintillator mixtures.

Contents

I

Chapter 1

Neutrino oscillations

1.1 Introduction

Neutrinos are the most abundant matter particles in the universe. But as they possess neither electrical charge nor color, they can only interact weakly with other particles, which makes them nearly invisible. But in spite of their very rare interactions, they play a decisive role in many of nature's phenomena. For example, they take part in the radioactive β-decay

$$n^0 \longrightarrow p^+ + e^- + \bar{\nu}_e. \tag{1.1}$$

In a two-particle process, with only an electron and a proton created, the continuous beta spectrum would violate the conservation of energy. Because of the particle spins involved in the reaction, angular momentum conservation would also be violated. In fact, it was the β-decay that led to the postulation of neutrinos by W. Pauli in 1930. Its counterpart, the inverse β-decay

$$\bar{\nu}_e + p^+ \longrightarrow n^0 + e^+, \tag{1.2}$$

then delivered the experimental proof of neutrino existence. F. Reines and C. L. Cowan observed this reaction in 1956 with reactor neutrinos in a liquid scintillation detector [1].

In astrophysics, neutrinos were found to be the ideal probe to study the solar interior. While photons would need several thousand years to diffuse through the dense plasma, neutrinos traverse the sun's radius with essentially the speed of light. In 1968 R. Davis measured the solar neutrino flux with help of a radiochemical detector [2]. As only a fraction of the expected flux was found, this experiment gave a first experimental hint of neutrino oscillations. This possibility has already been suggested theoretically by B. Pontecorvo in 1957 [3]. The oscillation theory has then been fortified by the experimental findings during the following decades and finally been proven by the results of several neutrino oscillation experiments.

1.2   Neutrino oscillation principles

The key requirement for neutrino oscillations to occur is that flavor and mass eigenstates do not coincide. The set of flavor eigenstates $|\nu_\alpha\rangle$ and the set of mass states $|\nu_k\rangle$ form two distinct bases of the Hilbert space. The change of basis is done by a matrix U. As both sets are orthonormal [4], U has to be a rotation matrix and is thus orthogonal in the real case or unitary in the complex case. A quantum mechanical observation consists of essentially three steps: The initial particle creation (or preparation), its propagation in time and space, and finally its detection. A neutrino generated in a certain flavor state $|\nu_\alpha\rangle$ is a superposition of the mass eigenstates and can be represented as

$$|\nu(0)\rangle = |\nu_\alpha\rangle = \sum_k U_{\alpha k} |\nu_k\rangle \qquad (1.3)$$

The time evolution of $|\nu_\alpha\rangle$ during its propagation is given by

$$|\nu(t)\rangle = \sum_k e^{-iE_k t} U_{\alpha k} |\nu_k\rangle . \qquad (1.4)$$

Here, E_k is the relativistic energy of the neutrino ν_k. The presence of the energies E_k in (1.4) is important: It means that the mass eigenstates $|\nu_k\rangle$ evolve differently due to their different masses m_k. The contributions of the different mass eigenstates change during the time the neutrino travels. This is the essence of the oscillation phenomenon.

Finally, at the moment of its detection the evolved state $|\nu(t)\rangle$ is projected onto the final state $\langle\nu_\beta|$.

$$\langle\nu_\beta \,|\, \nu(t)\rangle = \sum_n \langle\nu_n| U_{n\beta}^\dagger \cdot \sum_k e^{-iE_k t} U_{\alpha k} |\nu_k\rangle = \sum_k e^{-iE_k t} U_{\alpha k} U_{\beta k}^\star . \qquad (1.5)$$

The *oscillation probability* $P_{\alpha\to\beta}$, i.e. the probability to detect an original $|\nu_\alpha\rangle$ neutrino as a $|\nu_\beta\rangle$, is now given by the squared modulus of the quantum-mechanical amplitude (1.5) [1]. One obtains

$$
\begin{aligned}
P_{\alpha\to\beta} = |\langle\nu_\beta \,|\, \nu(t)\rangle|^2 &= \left| \sum_n e^{-iE_n t} U_{\alpha n} U_{\beta n}^\star \right|^2 = \\
&= \sum_{m,n} \left| U_{\beta m} U_{\alpha m}^\star U_{\beta n}^\star U_{\alpha n} \right| \cos\left[(E_\alpha - E_\beta)\, t - \arg\left(U_{\beta m} U_{\alpha m}^\star U_{\beta n}^\star U_{\alpha n} \right) \right]
\end{aligned}
\qquad (1.6)
$$

for the probability to oscillate from $|\nu_\alpha\rangle$ to $|\nu_\beta\rangle$. E_k is the total energy of the respective neutrino. The more complicated expansion on the second line already

---

[1]Of course, this requires that the reaction to detect the $|\nu_\beta\rangle$ is energetically possible. Otherwise *oscillation probability* and *detection probability* are not equivalent.
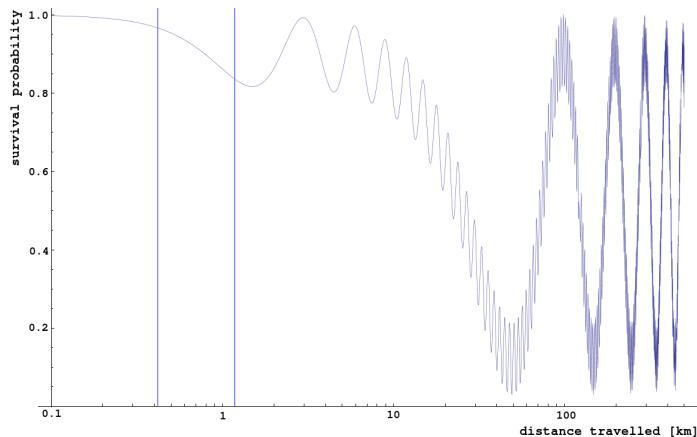
Figure 1.1: Survival probability for 3 MeV initial electron neutrinos as functions of the distance from the point of creation. The values used in this graph are $\sin^2 2\theta_{12} = 0.87$, $\Delta m_{12}^2 = 7.59 \cdot 10^{-5}$ eV^2 and $\Delta m_{13}^2 \approx \Delta m_{23}^2 = 2.5 \cdot 10^{-3}$ eV^2; a value of $\sin^2 2\theta_{13} = 0.18$ has been assumed.

takes the possibility of a complex mixing matrix into account; for a completely real matrix the argument becomes zero. The probability $P_{\alpha \to \alpha}$ to find the original flavor state is called the *survival probability*.

Especially for phenomenological considerations it is now useful to express this equation with help of other parameters. To do so, we use the fact that neutrinos can always be regarded ultra-relativistic particles because of their tiny masses and the typical energies involved in their production process. This peculiarity has two consequences: First, the relativistic energy-momentum relation can be approximated as

$$E_k = \sqrt{\mathbf{p}^2 + m_k^2} \approx p + \frac{m_k^2}{2p} \approx E + \frac{m_k^2}{2E}, \tag{1.7}$$

where $p = |\mathbf{p}|$. Second, neutrinos travel essentially at the speed of light c and the time t can be replaced by the distance travelled L. The oscillation probability (1.6) can now be written as

$$
\begin{aligned}
P_{\alpha \to \beta} &= \left| \sum_n e^{-i \frac{m_n^2}{2E} L} \, U_{\alpha n} U_{\beta n}^\star \right|^2 = \\
&= \sum_{m,n} |U_{\beta m} U_{\alpha m}^\star U_{\beta n}^\star U_{\alpha n}| \cos\left[\left(\frac{\Delta m_{mn}^2}{2E} L \right) - \arg\left(U_{\beta m} U_{\alpha m}^\star U_{\beta n}^\star U_{\alpha n} \right) \right]
\end{aligned}
\tag{1.8}
$$

at a distance L from the point of creation. Δm_{mn}^2 is the difference of the squared

masses of the mass eigenstates $|\nu_m\rangle$ and $|\nu_n\rangle$. The survival and oscillation probabilities in the three-neutrino case are illustrated in fig. 1.1.

The *mixing angle* θ is part of the oscillation amplitude. $\theta = 0$ would mean that the survival probability always remains 100 %, while $\theta = 45°$ means maximal oscillations. The oscillation frequency is a function of the average particle energy E and the squared mass difference Δm_{mn}^2 of the neutrino types.

It is evident from (1.8) that ν-oscillations require that not all neutrinos have the same mass. In particular, they cannot be massless altogether. If this was the case, all Δm_{mn}^2 would be zero and consequently $P_{\alpha \rightarrow \beta}$ would be as well. So the existence of neutrino oscillations is also a proof of non-zero neutrino masses. A second consequence of oscillations is that the lepton flavor number L_α is not conserved in this phenomenon.

1.3 The neutrino mixing matrix

For the particular form of the mixing matrix U one has to consider the three neutrino types. The three families require a 3×3-matrix. Furthermore, the complete matrix contains complex phase factors to account for the Dirac or Majorana nature of neutrinos and for the possibility of CP-violation. The mixing matrix is called PMNS matrix[2]. In its standard parametrization, the PMNS matrix is written as follows:

$$\begin{pmatrix} U_{e1} & U_{e2} & U_{e3} \\ U_{\mu 1} & U_{\mu 2} & U_{\mu 3} \\ U_{\tau 1} & U_{\tau 2} & U_{\tau 3} \end{pmatrix} = \begin{pmatrix} 1 & 0 & 0 \\ 0 & \cos\theta_{23} & \sin\theta_{23} \\ 0 & -\sin\theta_{23} & \cos\theta_{23} \end{pmatrix} \begin{pmatrix} \cos\theta_{13} & 0 & \sin\theta_{13}\,e^{-i\delta} \\ 0 & 1 & 0 \\ -\sin\theta_{13}\,e^{i\delta} & 0 & \cos\theta_{13} \end{pmatrix} \cdot$$

$$\begin{pmatrix} \cos\theta_{12} & \sin\theta_{12} & 0 \\ -\sin\theta_{12} & \cos\theta_{12} & 0 \\ 0 & 0 & 1 \end{pmatrix} \begin{pmatrix} e^{i\alpha_1/2} & 0 & 0 \\ 0 & e^{i\alpha_2/2} & 0 \\ 0 & 0 & 1 \end{pmatrix} \tag{1.9}$$

Here, the Dirac or Majorana character of neutrinos is accounted for by the two phases α_1 and α_2. They are zero exactly if neutrinos are Dirac-particles, which is still an open question. However, they are irrelevant for oscillation phenomena; these are controlled by the three mixing angles θ_{12}, θ_{23} and θ_{13}, as well as by the squared mass differences Δm_{mn}^2 and the CP-violating phase δ.

Only the mixing angles θ_{12} and θ_{23} and the mass differences Δm_{12}^2 and Δm_{23}^2 are known at present. It is convenient to refer to expressions of the type $\sin^2 2\theta_{13}$

---

[2]Named after Pontecorvo, Maki, Nakagawa and Sakata.

instead of the mixing angles themselves, as these are directly connected to the oscillation probabilities (see section 1.5). θ_{12} has been measured in experiments with solar and reactor neutrinos. The value $\sin^2 2\theta_{12} = 0.87 \pm 0.03$ was obtained from the solar and KamLAND data [5, 6]. θ_{23} was determined in atmospheric and accelerator experiments. The Super-Kamiokande collaboration reported the currently best limit, being $\sin^2 2\theta_{23} > 0.92$ at 90% confidence level [6, 7]. Within the uncertainty this value is compatible with $45°$, i.e., the oscillation probability could be maximal. If this is confirmed in the future, this could be a hint towards an underlying symmetry. However, a global fit to the data indicates that $\sin^2 2\theta_{23} = 0.996 \, ^{+0.004}_{-0.030}$ [8].

1.4   Open questions

θ_{13} is the last unknown mixing angle. The current best upper limit comes from the Chooz experiment and was found to be $\sin^2 2\theta_{13} < 0.19$ at 90 % confidence level [9].

There are some hints for a non-vanishing value of θ_{13}. Though there is no compelling evidence for a non-zero θ_{13} from a direct measurement, a global fit over the available neutrino data performed by Fogli et al. indicates $\sin^2 2\theta_{13} = 0.08 \pm 0.04$ [10]. It includes data from solar, atmospheric and accelerator experiments as well as data from the reactor experiments Chooz and KamLAND, and recent data from the MINOS accelerator experiment. A fit to the KamLAND and solar neutrino data, including new results from SNO, yields a best fit value of $\sin^2 2\theta_{13} = 0.08 \, ^{+0.08}_{-0.06}$ [11].

Investigation of CP-violation

Equation (1.6) describes the oscillation probabilities for neutrinos. For antineutrinos the respective entities have to be conjugated and $\bar{\nu}$-oscillations are controlled by $U^\star$. If at least one of the phases δ, α_1 or α_2 is not zero, the mixing matrices U and $U^\star$ are not identical, which would manifest in a different behavior of ν and $\bar{\nu}$. This would be a violation of CP-conservation. As the Majorana-phases α_j have no influence on oscillations, possible differences between the oscillation probabilities of ν and $\bar{\nu}$ can be attributed to δ. It can be seen in (1.9) that δ always appears together with θ_{13}, so θ_{13} has to be known in order to be able to measure δ. The knowledge of θ_{13} is consequently the basis of a thorough investigation of CP-violations in the lepton sector. The case of $\theta_{13} = 0$, on the other hand, would also mean that there are no differences in ν- and $\bar{\nu}$-oscillations, i.e., oscillations would be CP-conserving.

The CP-phase δ itself may be of fundamental importance for the understanding of the universe. The theory of leptogenesis assumes that the observed dominance of matter over antimatter in the universe was mediated by an asymmetry

in the leptonic sector. In such a scenario, δ could have had a decisive role in the early stages of the universe [12].

Extensions of the Standard Model

As discussed earlier, there are many reasons to believe that an extension of the Standard Model is necessary. The origin of the small neutrino masses is only one open question. Another issue is the large number of free parameters, which is dissatisfying for such a fundamental theory. At least 25 parameters, including neutrino masses and mixing parameters, have to be determined experimentally and cannot be deduced within the framework. In an attempt to reduce the number of input parameters, the various new models proposed try to predict the mixing angles and make individual statements for θ_{13} [13]. An experimental value - or a better upper limit - could sort out many theories and guide theorists towards a valid extension of the Standard Model.

Neutrino mass and mass hierarchy

The absolute neutrino masses are still unknown, and much of what is known about them was learned from oscillations. As shown in section 1.2 the oscillation probabilities depend on the differences in the squared neutrino masses Δm_{ij}^2. However, the neutrino mass hierarchy is still unknown. Δm_{12}^2 is positive, which is known from solar neutrinos and matter effects. This allows a normal or inverted hierarchy (if m_1 and m_2 are not degenerated). But which of the two options is realized depends on the sign of $\Delta m_{23} \approx \Delta m_{13}$, which is unknown.

The absolute neutrino masses have to be determined separately. The currently best upper limit for the effective $\bar{\nu}_e$-mass

$$m_{\bar{\nu}_e}^{\text{eff}} = \sqrt{\sum |U_{ei}|^2 \, m_{\nu_i}^2} \qquad (1.10)$$

is 2.3 eV at 95 % CL [14]. This value comes from the tritium β-decay. Astronomical constraints on $m_{\bar{\nu}_e}^{\text{eff}}$ from the 1987 supernova indicate $m_{\bar{\nu}_e}^{\text{eff}} < 5.7$ eV at 95 % CL [15]. A promising candidate to discover the effective $\bar{\nu}_e$-mass is the β-spectrometer KATRIN with a projected sensitivity down to 0.2 eV. The KATRIN experiment also employs the tritium β-decay and is to begin data taking in the near future [16]. Another approach, the micro-calorimeter experiment MARE, currently in R&D phase, may reach a similar sensitivity [17]. It is worth noting that the above cases exclusively consider $\bar{\nu}_e$s; the best upper limit for an effective ν_e mass comes from electron capture on ^{163}Ho and is 225 eV [18, 19]. It could differ from the effective $\bar{\nu}_e$ mass in case of Dirac-type neutrinos and CPT violation.

1.5 Measuring θ_{13}

The reactor neutrino experiments Double Chooz, Daya Bay, and RENO to determine θ_{13} are currently under construction. Neutrinos from nuclear reactors have been found ideally suited for an experiment on θ_{13}. The reaction products created from nuclear fission have a neutron surplus and in the following beta decays electron antineutrinos $|\bar{\nu}_e\rangle$ are created and emitted isotropically. Here, this distinction between $|\nu_e\rangle$ and $|\bar{\nu}_e\rangle$ is important because of the MSW-effect: the $|\nu_e\rangle$s are subject to coherent forward scattering off electrons due to charged current interaction. This modifies the oscillation probabiliy of $|\nu_e\rangle$s when they propagate through matter. The MSW-effect does not influence $|\bar{\nu}_e\rangle$s, as they would require positrons to undergo charged current coherent forward scattering. As the $|\bar{\nu}_e\rangle$s are not subject to the matter effect, their oscillations can be treated like vacuum oscillations and the equations of section 1.2 apply. Accelerator experiments working with $|\nu_e\rangle$s have to take this effect into account, which makes data analysis more complex.

In the three reactor experiments mentioned above one searches for a (possible) deficit in the $|\bar{\nu}_e\rangle$ flux. Using the parametrization (1.9) for the calculation of the survival probability (1.8), the case of an initial $|\nu_e\rangle$ is described by

$$
\begin{aligned}
P_{\bar{\nu}_e \to \bar{\nu}_e} = 1 &- 4\cos^2\theta_{12}\cos^4\theta_{13}\sin^2\theta_{12}\ \sin^2\left(\frac{\Delta m_{12}^2}{4E}L\right) \\
&- 4\cos^2\theta_{12}\cos^2\theta_{13}\sin^2\theta_{13}\ \sin^2\left(\frac{\Delta m_{13}^2}{4E}L\right) \\
&- 4\sin^2\theta_{12}\cos^2\theta_{13}\sin^2\theta_{13}\ \sin^2\left(\frac{\Delta m_{23}^2}{4E}L\right)
\end{aligned} \tag{1.11}
$$

If the detectors are placed close to the reactor, the oscillation $\bar{\nu}_e \to \bar{\nu}_\mu$ is negligible due to the very small Δm_{12}^2. In this case, the first term can be neglected. Furthermore, since $\Delta m_{13}^2 \approx \Delta m_{23}^2$, the second and third term can be combined. One then gets

$$
\begin{aligned}
P_{\bar{\nu}_e \to \bar{\nu}_e} =&1 - (2\cos\theta_{13}\sin\theta_{13})^2\ \sin^2\left(\frac{\Delta m_{23}^2}{4E}L\right) \\
=&1 - \sin^2 2\theta_{13}\ \sin^2\left(\frac{\Delta m_{23}^2}{4E}L\right).
\end{aligned} \tag{1.12}
$$

This is a relatively simple expression, where θ_{13} can be determined from four parameters, of which Δm_{23}^2 is known, L can be set by positioning the detector, and E and $P_{\bar{\nu}_e \to \bar{\nu}_e}$ can be measured in the experiment. This allows for a very "clean" measurement of θ_{13}. This is a great advantage over long baseline experiments like NOνA and T2K, which have to consider more parameters and are more prone to

parameter correlations and degeneracies.

However, if $\sin^2 2\theta_{13}$ is smaller than 0.01, reactor neutrino experiments may be overstrained. In such a scenario, β-beams and neutrino factories may be the weapon of choice. But prior to such experiments the results of the current projects are being awaited, as they help further planning.

Chapter 2

The Double Chooz scintillators

2.1 The Double Chooz experiment

Double Chooz is a reactor neutrino experiment designed to measure $\sin^2 2\theta_{13}$ with a sensitivity down to 0.03 at 90 % CL [20]. The experiment is performed at the Chooz nuclear power plant. The plant's two reactors provide a thermal power of 4.27 GW each, with a total neutrino flux of $8 \cdot 10^{20}$ neutrinos per second. Double Chooz is a disappearence experiment. It measures the $\bar{\nu}_e$-flux at a distance L of the neutrino source and compares it to the flux predicted for $\theta_{13} = 0$. If a statistically significant deficit is measured, θ_{13} can be determined from the data obtained.

Double Chooz employs two identical liquid scintillation detectors in different distances from the nuclear reactors. The use of two detectors makes the experiment in principle independent of the knowledge of the reactor power, as the neutrino flux through one detector can be measured relative to the flux through the other. This reduces the experimental uncertainties coming from the reactor power output. The projected total systematic error is 0.6 %, compared to 2.7 % in the Chooz experiment [20], which measured the best limit on θ_{13} to date. Due to a measurement time of 5 years and a larger fiducial mass, Double Chooz is also expected to reduce the statistical error from 2.8 % to 0.4 %. The far detector is currently being built at a mean distance of 1.05 km from the reactors, the near detector will have a mean distance of 415 m. The far detector is located underground with an overburden of 300 m w.e., the near detector will have an overburden of ca. 75 m w.e. The detector positions are approximately such that the near detector sees an unoscillated $\bar{\nu}_e$ spectrum, while the far detector resides at a distance where the survival probability reaches the first minimum. It is located underground. For both distances the influence of the other two mixing angles is negligible. Fig. 1.1 in section 1.2 shows the location of the Double Chooz detectors and the $\bar{\nu}_e$ survival probability.

Figure 2.1: Schematic view of the detector structure. In the center the transparent acrylic vessels for the Target and Gamma Catcher can be seen. They are surrounded by the photomultiplier tubes mounted on the buffer tank. The Inner Veto volume follows behind the buffer.
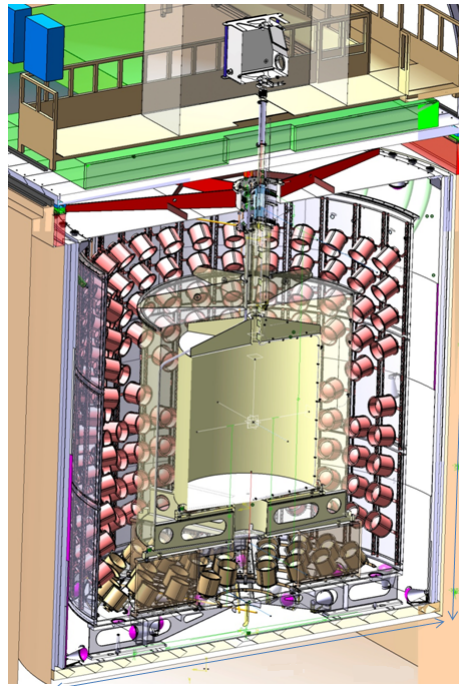
The reaction channel for neutrino detection is the inverse beta decay. Electron antineutrinos from the reactors react with a proton of the liquid scintillator and produce a positron and a neutron as in (1.2). The positron creates scintillation light while it loses energy during its passage in the fluid (see chapter 3). It then annihilates with an electron into two 511 keV photons, which themselves create scintillation light via the production of Compton-electrons. The light created by the positron constitutes the *prompt signal*. The neutron is detected indirectly. For an efficient detection, the scintillator is loaded with an organic gadolinium complex. The neutron first thermalizes in collisions with protons of the medium and after about 30 μs it is captured by a Gd-nucleus. The excited nucleus rapidly decays via emission of typically three or four gamma photons with a total energy of about 8 MeV. These photons then lead to the production of a second scintillation pulse, the *delayed signal*. The neutrino signature therefore consists of two scintillation pulses that are typically less than 200 μs apart. These events are searched for and identified as neutrino events if both signals pass the applied detection cuts. The cuts utilize the energy of the prompt signal (over 1 MeV from the e^+ annihilation) and delayed delayed signal (8 MeV from the Gd-deexcitation), and the time correlation of the two events (200 μs).

The detector itself is a large-volume liquid scintillation counter. Each detector is divided into four sections of concentric cylindrical volumes. The structure can be seen in fig. 2.1. The innermost volume is the neutrino target, where the inverse beta decay reactions are detected. It is filled with the gadolinium-loaded

organic liquid scintillator for neutron capture. The gamma quanta produced in the gadolinium deexcitation and positron annihilation have to be converted into visible light by the scintillator mixture (see chapter 3 for details). If a gamma photon escapes the target, it can be detected in the Gamma Catcher (GC) volume surrounding the target. It contains 22.3 m^3 of an unloaded liquid scintillator. The target and GC vessels are acrylic containers, which are transparent in the wavelength region of the scintillation light. The following volume is the buffer. It contains 114 m^3 of non-scintillating liquid, which protects the target and GC volumes from radioactivity mainly coming either from the surrounding rock or from the PMT glass. The buffer vessel is a steel tank, which also serves as a support structure for the 390 photomultiplier tubes (PMTs) observing the scintillations coming from the fiducial volume. The steel tank also optically separates these three volumes from the Inner Veto (IV), the fourth and outmost volume of the detector. The veto is an active protection against cosmic muons that are not stopped in the detector overburden. It consists of 90 m^3 of an organic liquid scintillator which is observed by another 72 PMTs. Muon events are detected by the scintillation light created when it traverses the IV. To complete the veto system, an Outer Veto is installed on top of the detector. It consists of multiple layers of plastic scintillator panels extending over an area larger than the detector, which provide tracking information for traversing muons. Purpose of the Outer Veto is to identify muons which miss the IV and create high-energy secondary particles close to the detector, since these could diffuse to the sensitive volumes and fake neutron events.

2.2 Liquid scintillators in Double Chooz

A major improvement in respect to the first Chooz experiment is the use of newly developed scintillator mixtures. Especially the development of a novel gadolinium-loaded target scintillator was a core requirement for the whole project. The target and GC scintillators were developed and produced at the Max-Planck-Institut für Kernphysik (MPIK) [21, 22].

Target

The target scintillator medium is a mixture of 80 % n-dodecane and 20 % *phenyl-o-xylylethane* (PXE). Using a mixture of solvents gives the possibility to adjust properties. The composition chosen combines high transparency and scintillation performance with high chemical compatibility of the materials.

Dodecane is highly transparent for the wavelengths of the scintillation light and is highly compatible with the materials used. It also has a high proton density and thus increases the probability for the inverse beta decay reaction on protons. A great advantage of using dodecane rather than a mineral oil, is that dodecane

is a well defined chemical and the number of protons can be determined precisely. The proton number is important for the calculation of the $\bar{\nu}_e$ reaction probability, which directly influences the error of the θ_{13} measurement in the first phase of the experiment, where there is only one detector. In contrast, a mineral oil is a mixture of different compounds and the error on the proton number may be significantly larger. As PXE has a higher light yield than dodecane, 20 % PXE are added to the mixture to increase the light output [23, 24]. However, PXE is aggressive to the acrylics and cannot be added in high concentrations. The 20:80 relation of PXE to dodecane has been tested and proven to be compatible with the acrylics on a long-term scale. PXE is commercially available, but is not produced with the same high purity as dodecane. It was hence filtered in a column purification process, which could significantly augment the transparence of PXE especially in the higher wavelength region.

The primary fluorescent molecule (short *fluor*) used is *2,5-diphenyloxazole* (PPO), which is dissolved in the dodecane/PXE-mixture at a concentration of 7 g/l. The secondary fluor is *1,4-bis(2-methylstyrylbenzene)* (bis-MSB), at a concentration of 20 mg/l, which shifts the scintillation emission spectrum to higher wavelenghts. Details of the role of the fluors in the scintillation process can be found in section 3.2.

Main component of the target scintillator is the organic gadolinium complex. Natural gadolinium comes in several stable isotopes, of which each has a neutron capture cross section σ between 1.5 b and 254000 b, compared to $\sigma = 0.3$ b for thermal neutron capture on ^{1}H. The resulting mean cross section of gadolinium is roughly 10^5 times higher than for hydrogen. With the associated short capture time and the high decay energy (8 MeV) of an excited nucleus, gadolinium is ideally suited for an effective neutron detection. However, gadolinium itself is not soluble in the organic scintillator liquid. Therefore it is used in the form of Gd(thd)$_3$, an organic complex where three di(pivaloyl)methane ligands bind to the central Gd-atom. The β-diketone thd provides high solubility and chemical stability of the complex. The use of β-diketones in neutrino experiments is based on the work of F. X. Hartmann and R. A. Naumann [18]. They were then studied for use in scintillation detectors [25, 26]. The Gd(thd)$_3$ complex has shown to provide the high stability required for the project. It also could be sublimated to achieve a high radiopurity. The target scintillator is loaded with 1 g/l gadolinium in the form of the organic complex.

Finally, the target scintillator contains tetrahydrofuran (THF) as an additive. Small quantities (ca. 0.25 %$_{vol}$) of THF increase the solubility of Gd(thd)$_3$ in the scintillator and protects the complex from adsorption of other molecules. The latter is a crucial point, since adsorptions may deteriorate the scintillator and long-term stability is a key requirement of the scintillator.

Gamma Catcher

The Gamma Catcher is also an organic liquid scintillator, but does not contain the Gd-complex. The GC mixture was also produced at the MPIK. In the development of the GC the focus laid on other requirements than those of the target. It primarily had to be made sure that the density of the GC matches the target density. This is important to avoid mechanical pressure on the acrylic vessels. Furthermore, the transparency for scintillation light has to be ensured. This could be achieved with a paraffinic/naphtenic mineral oil, the medicinal white oil Ondina 909 by Shell. It can be produced very clean and is transparent in the wavelength region of the scintillation light. It is also very compatible with the acrylics. Together with dodecane and PXE the GC mixture has been carefully adjusted to match the target in density. The GC composition contains about 66 %$_{\text{vol}}$ Ondina 909, 30 %$_{\text{vol}}$ dodecane and 4 %$_{\text{vol}}$ PXE. The use of a mineral oil with high uncertainties in the proton number is possible for the Gamma Catcher, since it is not part of the fiducial volume.

As the event energy will be reconstruced from the light output in the analysis phase of the experiment, a gamma quantum has to produce equal amounts of light, independent if it causes scintillations in the Target or in the Gamma Catcher. Studies concerning this aspect have been carried out [24] and led to a GC composition where the concentration of PPO is 2 g/l. However, the option of having a primary fluor concentration of 5 g/l is still reserved. The reason for having this backup option will become clear after chapter 3 and is discussed in section 6.1. The secondary fluor is again bis-MSB at 20 mg/l.

Inner Veto

Since it has a high light yield and the distances to the PMTs are comparatively small, a high attenuation length of the liquid is not so critical as in the case of the other scintillators, which gives more freedom to compose the mixture. The IV scintillator is a mixture of 37.5 % *linear alkyl benzene* (LAB), 62.5 % tetradecane, 3 g/l PPO and 20 mg/l bis-MSB. It is characterized by a fast scintillation time and high light output.

The inner veto volume is the only detector component which differs in the two Double Chooz detectors. The near detector will have less overburden and is hence exposed to a higher muon flux. This is compensated with a larger IV volume.

Buffer

Although the buffer liquid is not a scintillator, the buffer volume is shortly described here for completeness.

The buffer vessel is also the support structure for the PMTs. Although they are manufactured from low-radioactivity glass, the PMT covers are still an im-

portant source of radioactive background. The buffer liquid is therefore used to protect the GC and Target volumes from background radiation coming from the PMTs or farther outside. Apart from the chemical compatibility and right density, the requirements of the buffer liquid are high transparency and radiopurity. They are fulfilled by utilizing a non-scintillating mineral oil.

Chapter 3

Scintillation in liquids

The use of liquid scintillators has a long tradition in neutrino physics and goes back to the times of Reines and Cowan, who discovered the neutrino in a liquid scintillator tank [1]. Since then, liquid scintillation technology has seen some important progresses. Most notably are the rise of highly efficient scintillating compounds on one hand and the development of soluble organic metal complexes on the other. Both trends fortified the usefulness of liquid scintillators in particle physics. They can be produced in large quantities with relatively low costs, which makes them a common choice for large-volume detectors.

The simplest liquid scintillators consist of small concentrations of a fluorescent substance (called *fluor*) dissolved in an organic liquid. Pure liquid scintillators, consisting only of a scintillating solvent (e.g. benzene or xylene), would lose a considerable amount of the produced light due to self-absorption. The fluors solve this problem by emitting light at wavelenghts higher than the absorption region of the solvent. In this way the re-absorption can be significantly reduced. The solvent's main purpose then becomes the conversion of the kinetic energy of the incident particle into electronic excitational energy, while the fluors capture the excitation energy and are responsible for light production. Typical fluor concentrations vary in the range of a few grams per liter. Along with the primary fluor, additional secondary fluors can be added as wavelength shifters. They are used to shift the scintillation spectrum further away from the solvent's absorption band and towards the sensitive wavelength region of the PMT. According to the number of its active components a scintillator is classified as *unary, binary, ternary*, and so on. Further additives, like stabilizing agents or - for example in the case of Double Chooz - organic metal complexes, may be added to suit the scintillator for advanced purposes.

3.1 Formation of excited states and scintillation

In the domain of organic scintillators, fluorescent materials are aromatic compounds. Their key feature are aromatic rings. These are unsaturated circular arrangements of carbon atoms, held together by conjugated double bonds. The important characteristic of an aromatic ring is that the wave functions of the valence electrons are delocalized over the entire ring structure. They form π-orbitals above and below the molecular plane (fig. 3.1a). Loosely speaking, a π-electron belongs to the entire molecule rather than to a specific atom. It is mainly in these π-orbitals where scintillation occurs. For illustration, a typical level scheme of a π-orbital is given in fig. 3.1b. The six electrons in the orbital are spin paired, so the ground state is necessarily a singlet state, denoted S_0. Directly above the ground state lie the associated vibrational energy substates. In some distance follows the first excited singlet state S_1, together with its vibrational band. Further singlet states follow at higher energies. The excited triplet states display a similar configuration [27]. The transition responsible for the emission of fluorescence light is $S_1 \rightarrow S_0$, from the first excited singlet state to the ground state [28]. Other transitions of the general form $S_n \rightarrow S_0$ have been found to be non-radiative [29]. The $T_1 \rightarrow S_0$ transition is suppressed by the selection rules. It therefore has a much longer lifetime and is responsible for phosphorescence.
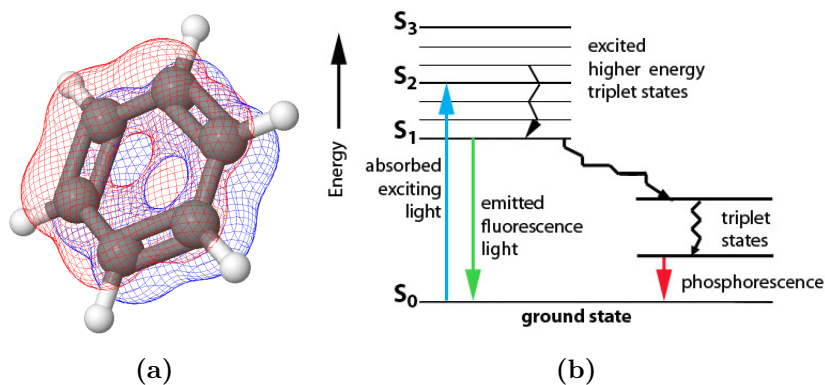

(a) (b)

Figure 3.1: (a) π-orbitals in the benzene molecule, the most basic aromatic compound. It can be seen that they extend over the ring and that they are positioned above and below the molecular plane. (b) Qualitative level scheme of the benzene molecule. The processes of fluorescence and phosphorescence, as well as internal conversion from higher states to the S_1 state are illustrated.

Formation of excited states

Upon excitation by an incident particle, direct excitation of the first states S_1 or T_1 is suppressed by symmetry and spin arguments respectively [30]. The molecules are mainly excited into the higher electronic states S_n and T_n by direct excitation and ion recombination respectively [30]. After that, the S_1 and T_1 states are populated by internal conversion processes.

Singlet states are primarily formed when the incident particle's energy loss dE/dx is small [30]. The higher excited singlets S_n degrade rapidly by internal conversion.[1] This degradation takes place very fast with a time constant of about 10^{-12} s and after several picoseconds essentially all excited singlets are in the S_1 state [28]. Triplet states can be created upon the recombination of ions with free electrons or by intersystem-crossing. The direct decay into the S_0 state is suppressed because of the selection rules and the decay takes place on phosphorescence time scales [28]. A more efficient mechanism are triplet-triplet interactions, in which one molecule returns to its ground level S_0, whereas the other one emerges in the S_1 state. The decay now follows the scheme described above [27]. The postponed population and deexcitation of S_1 states through this mechanism cause a delayed component in the scintillation emission. Together, the prompt and delayed parts constitute the scintillation pulse shape. As each particle type may create a different ratio of singlet and triplet states, the characteristic scintillation pulse shapes vary with the incident particle. This allows for the powerful technique of pulse shape discrimination.

3.2   Energy transfer

As the solvent constitutes the bulk matter of the mixture, primarily solvent molecules are excited when an ionizing particle traverses the scintillator. The excitational energy then has to be distributed to the solutes. An effective energy transfer is of great importance to the scintillation efficiency. The different mechanisms of energy migration are discussed in the following.

Energy transfer between solvent molecules

The mean life time of the singlet state S_1 is typically of the order of nanoseconds. This is enough time to allow an excited molecule to interact with its surroundings and to transfer its excitation energy to a molecule in its vicinity. In this way the excitations migrate between the solvent molecules over several molecular

---

[1]Note that the term *internal conversion* applies to the chemical process of radiationless decay of excited states. The excitation energy is dissipated into thermal energy. It is totally different from the physical process of radioactive internal conversion.

distances. When the excitation energy reaches a fluor molecule, it can be captured and converted to fluorescence light. The main process to account for energy transfer from one solvent molecule to another is the formation of excitons [31].

Solvent molecules in their ground states normally do not develop bondings between each other. In an excited state however, a molecule may have an electronic wave function such that it can constitute a metastable bound state with an adjacent unexcited solvent molecule. Such excited dimers (or *excimers*) are very short-lived. Upon breaking up, the excitation energy can remain with the previously unexcited molecule, which then forms an excimer with the next unexcited molecule and so on. In the literature, this process is referred to as *"hopping"* or *"migration transfer"* [32]. In organic liquid scintillators this process is probably the most important one. Though, it requires the two molecules in question to be oriented in parallel. If this is not the case, a molecule can transfer its energy via Coulombic octupole interactions [33, 34].

Energy transfer from solvent to the primary fluor

This phase of energy migration is governed by the so called Förster transfer [35] or FRET[2]. This is a non-radiative energy transfer process from a donor molecule to a different acceptor molecule through dipole-dipole interaction. An overlap of the donor's emission spectrum and the acceptor's absorption spectrum is a prerequisite to the process, in which a modest redshift of the acceptor spectrum is favorable for the transfer efficiency [36]. Due to its dipole-dipole nature, the transfer efficiency decreases with r^{-6}. For like molecules, as in the solvent-solvent transfer, the process contracts to the excimer-transfer described above [31]. An extended treatment of the Förster effect, involving suppressed transitions, was undertaken by Dexter [37]. This theory also considers dipole-quadrupole interactions and electron exchange processes. A full investigation of molecular energy transfer employing quantum electrodynamics was later done by Andrews [38]. The Förster transfer arises as the short-range limit of this theory, while the long-range limit leads to radiative transfers. Though it was formerly believed that energy transfer in this phase is purely non-radiative [34], radiative transfer was later found to play a certain role in the process, albeit mostly a minor one [33].

The scintillation efficiency depends heavily on the solute concentration. The light output first increases rapidly with the amount of the fluor in the mixture, but then saturates when a certain concentration is reached. In this case the increased interaction rate between the fluor molecules leads to a significant *self-quenching*, where radiationless deexcitation by mutual interaction of the fluors competes with the scintillation transition [28].

---

[2]Förster resonance energy transfer

Energy transfer from primary to secondary fluors

When the excitation energy finally reaches a fluorescent molecule, it can deexcite via photon emission (with its individual quantum efficiency). The scintillation mechanism would then be complete. However, there remains the risk of photon absorption, especially if the scintillator volume is large. It is therefore important that the mixture is sufficiently transparent for the emission bands of the fluor, i.e. a minimal overlap of its emission spectrum and the absorption spectra of solvent, primary fluor or impurities is desired. As a partial overlap is hard to avoid, a secondary fluor is often added to minimize reabsorption losses. The secondary fluor should absorb mainly at the emission region of the primary fluor to reduce solvent re-absorption and then reemit light at higher wavelengths, shifting it away from the solvent's absorption band.

The emission and absorption spectra of the DC scintillator components are shown in fig. 3.2. Due to the respective overlaps, the energy transfer normally takes place from PXE to PPO to bis-MSB, which then emits in a wavelength region where reabsorption is minimal.
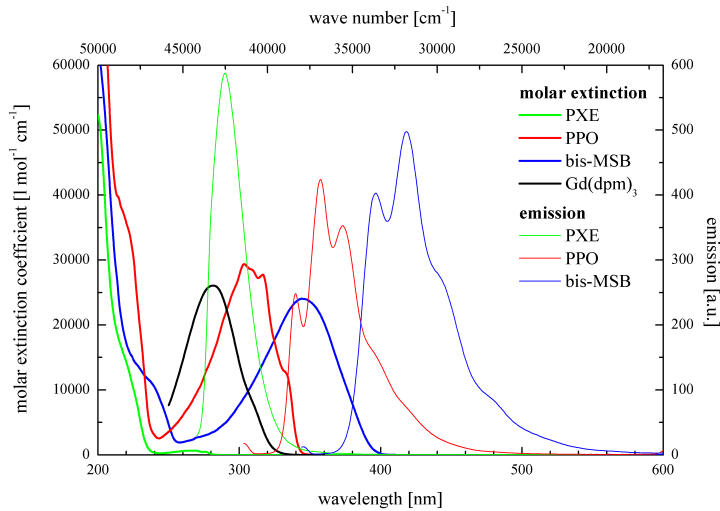
Figure 3.2: The emission and absorption bands of the DC scintillator components. The overlaps between primary and secondary fluor can be seen. The non-scintillating Gd-complex acts as a quencher. But the successive radiative energy transfer through PXE→PPO→bis-MSB shifts the wavelength away from the absorption bands.

3.3   Energy loss of electrons

As previously explained, the starting point of the scintillation process is the energy deposition of an ionizing particle in the scintillator material. Charged

particles interact electromagnetically with the electrons in the substance and lose their energy. In turn, the molecules are ionized or excited into higher electronic states. The specific energy loss, the amount of kinetic energy lost in a unit of length, is normally described by the Bethe-Bloch formula. Electrons however are a special case. The electron-electron interaction is a process between two quantum-mechanically indistinguishable particles. Their specific energy loss is given by the Berger-Seltzer formula [39]

$$\left(\frac{dE}{dx}\right) = 2\pi r_e^2 m_e c^2 n_e \beta^{-2} \left[\ln\left(2(\gamma+1)\frac{m_e^2 c^4}{I^2}\right) + F(\tau) - \delta\right], \qquad (3.1)$$

where m_e is the electron rest mass, r_e the classical electron radius, n_e the electron density, I the mean ionization energy of the medium and β and γ are the Lorentz variables of the electron in motion. The function $F(\tau)$ discriminates between electrons and positrons, as the latter are not subject to the indistinguishability considerations. For electrons $F(\tau)$ has the form

$$F(\tau) = 1 - \beta^2 + \ln\frac{\tau^2}{4} + \frac{\tau^2}{8\gamma^2} - \frac{2\tau+1}{\gamma^2}\ln 2,$$

with $\tau = \gamma - 1$ [40]. The density effect, which considers the shielding of the particle's Coulombic field due to induced polarizations, adds a term δ [41]. Besides the energy loss due to ionization described above there is also a contribution of bremsstrahlung which has to be taken into account. But at electron energies below 1 MeV, as they are considered in this document, both the density effect and bremsstrahlung are negligible.

3.4   Ionization quenching

The previous considerations only took into account energy transfer from excited to unexcited molecules. In this case, the energy is passed through the scintillator until it is either released as light or dissipates into heat. The interaction of two excited molecules may lead to mutual radiationless deexcitation and therefore to a loss of scintillation light. This is of special importance if the density of excitations and ionizations is very high, like at the end of the trajectory of an incident particle, where dE/dx is large. This type of quenching is called *ionization quenching*. It is intrinsic to any type of scintillator. Different processes are proposed to explain the ionization quenching effect on a molecular level.

3.4.1   Birks-model

Many models have been developed to quantitatively describe the reduction in light yield by ionization quenching. A commonly used model is the one by

Birks [28, 42]. It is principally motivated phenomenologically but still succeeds to characterize this effect well enough for many practical purposes. He originally developed this model for pure anorganic anthracene crystal scintillators and identifies crystal defects as the quenching centers. Nevertheless, it can be applied to other types of scintillators as well and still gives reasonable results. In consequence, his formula established itself as a standard for the characterization of scintillator response functions.

Starting point of all following reflections is the experimental observation that the specific fluorescence dL/dx is proportional to the specific energy loss dE/dx of the primary particle, as long as dE/dx itself is small. For electrons, this limit is of the order of 100 keV electron energy [28]. In the case of complete absence of quenching, the specific light yield is thus given by

$$\frac{dL}{dx} = S_0 \frac{dE}{dx} \tag{3.2}$$

with a proportionality constant S_0, which gives the light yield, i.e. the number of photons produced per unit of energy. In the case of quenching, (3.2) has to be corrected. Birks argues that an incident particle - besides the excited molecules - also creates quenching centers which can capture the energy without releasing it as light. Their number is proportional to dE/dx as well. The fraction q of molecules which emit light is then

$$q = \frac{N}{N + kB'\frac{dE}{dx}} = \frac{1}{1 + kB\frac{dE}{dx}} \tag{3.3}$$

where N is the number of excited light-emitting molecules, $B'\,dE/dx$ the number of quenching centers and k the probability that such a center receives the excitation energy.[3] The specific fluorescence (3.2) is then reduced by the factor q:

$$\frac{dL}{dx} = \frac{S_0 \frac{dE}{dx}}{1 + kB\frac{dE}{dx}} \tag{3.4}$$

A generalization of this formula was presented by Chou [43]. Instead of a unary crystal scintillator he regards binary systems and therefore needs to include a kind of energy transfer mechanism. He considers a nonradiative migration process with an efficiency that is proportional to the square of the excited particle density and, at the end of his reasoning, obtains

$$\frac{dL}{dx} = \frac{S_0 \frac{dE}{dx}}{1 + A\frac{dE}{dx} + B\left(\frac{dE}{dx}\right)^2}. \tag{3.5}$$

---

[3]In practice, the parameters k and B are handled as a single constant kB. In the literature the symbol k_B can sometimes be found instead, but of course this has nothing to do with the Boltzmann constant and should be avoided.

Birks commented that the best concordance of (3.5) with experimental results is obtained for $B = 0$, i.e. when the formula reduces to (3.4) again [28]. More recent studies have made similar observations: in fits with Chou's equation, the parameter A has to be fixed to 0 in order to obtain a non-zero value for B (see for example [44]). However, this may be no longer the case if the incident particles are heavy ions instead of light nuclei. In the context of the dark matter experiment AMS-02 the scintillator response function was tested in dependance of the specific ion charge and it is reported that (3.5) yielded significantly better results for heavier ions (with $15 < Z < 30$) than Birks' formula. However, beyond $Z = 30$ both models fail to give a good agreement with the observations made [45]. The experiment performed in this thesis investigates the scintillator response to electrons and the analysis can be limited to (3.4).

3.4.2 Wright-model

The approach by Wright [28,46] is based on a rate equation. While (3.4) only considers unimolecular quenching, a distinction between unimolecular and bimolecular quenching is made here. He suggests that the former is the predominant process in the case of incident electrons while the latter adds additional quenching to the scintillation output in the case of incident heavy particles. He identifies the Coulombic interaction of neighboring excited molecules as the source of the quenching. The combined effect of the two quenching mechanisms leads to a decay equation

$$d\epsilon = -(p + k + a\epsilon)\,\epsilon\,dt \qquad (3.6)$$

for the population of excited molecules, where $\epsilon \sim dE/dx$ is the number of excited molecules present. p and k are the decay rates due to fluorescence emission and unimolecular quenching respectively, and $a\epsilon$ is the rate of deexcitation due to bimolecular interactions. It is proportional to the number of excited molecules present. The specific light yield obtained by (3.6) is

$$\frac{dL}{dx} = \frac{p}{a}\ln\left(1 + \frac{a}{p + k}\frac{dE}{dx}\right). \qquad (3.7)$$

Some objections have been made to (3.7). Birks commented that the model fails to precisely describe experimental observations from experiments with α-particles [28]. And Kallmann and Brucker noted that the reasoning of Wright assumes that bimolecular quenching and fluorescence are in direct competition to each other, which would lead to an unobserved decrease of the scintillation decay time for α-particles in comparison to incident electrons [47]. Nevertheless, the Wright-model is used in investigations of the ionization quenching effect (e.g. in [48]).

3.4.3 Voltz-model

A more detailed approach is chosen by Voltz et al. [49]. It makes two improvements to the previous models. First, it turns its attention to the process of energy deposition, more precisely, to the explicit creation of secondary electrons (δ-rays) and the resulting spatial distribution of ionized and excited molecules. Second, it makes a difference between production and decay of excited singlet states S_1 on one hand and triplet states T_1 on the other. These two components cause a prompt and a delayed component respectively (see section 3.1).

Let me first consider the primary particle to be an ion, say an α-particle or a proton. The case of electrons will be discussed towards the end of this section. The incident particle creates a trail of primary ionizations and excitations along its path. Because the range of the Coulomb interaction extends over several molecular diameters (before it is shielded by induced polarizations [41]), the region of primary ionizations is a cylindrical column of radius R. Regarding the production of secondary particles, most δ-electrons created receive relatively small energies. They already have a high dE/dx at the beginning of their trajectory and lose their energy in the vicinity of the original trail. In this way they further increase the ionization density within the column. But if the primary particle transfers a sufficiently large amount of energy to a secondary particle, it can leave the column and deposit its energy away from the regions of high ionization density. The molecules excited along the trail of such an electron are distant from each other and quenching is negligible (see also the footnote on page 24). One can therefore distinguish two disjoint regions:

The ionization column Here the density of excited molecules is very high. They interact with each other and are subject to quenching. This region is populated by both singlet and triplet states (see section 3.1).

The region outside of the column In this regions fast δ-electrons create excited molecules in their singlet state, that are essentially isolated and not affected by quenching, except at the end of the track.

The quenching process itself is now modelled as follows. Either there is a superexcited molecule[4] present within a critical range r_c from a given molecule in the first excited state; then they both interact and deexcite non-radiatively. Or there is not and the molecule decays under photon emission with its quantum efficiency ϵ. The probability that there is no quencher in the respective distance is Poisson-distributed:

$$P \sim \exp\left(-2\frac{r_c}{\langle d \rangle}\right) = \exp\left(-B\frac{dE}{dx}\right),\qquad(3.8)$$

---

[4]A superexcited molecule is an ionized molecule where the electron released does not possess enough kinetic energy to stride away from the ion and can still be considered loosely bound

in which the mean distance $\langle d \rangle$ between two excited molecules is inversely proportional to dE/dx. As the number of excitations is again proportional to dE/dx one finally gets

$$\frac{dL}{dx} = S_0 \frac{dE}{dx} \exp\left(-B\frac{dE}{dx}\right).$$ (3.9)

This holds for molecules in regions of high ionization density. The total specific fluorescence consists of the contributions of the singlet states and triplet states respectively. While the triplet states basically only lie within the column, singlet states are encoutered in both regions. These within the column are subject to quenching and yield a contribution according to 3.9. The others remain unquenched and contribute with a linear term[5]. In total, the individual contributions add up to

$$\frac{dL}{dx} = S_0 \left[A_s^{(1)}(1-F)\frac{dE}{dx}e^{-B_s(1-F)\frac{dE}{dx}} + F A_s^{(2)}\frac{dE}{dx} + A_t \frac{dE}{dx}e^{-B_t\frac{dE}{dx}} \right].$$ (3.10)

Parameters indexed with s and t are due to singlet and triplet contributions respectively. The branching parameter F is of special significance. It determines what fraction of the excited molecules lies outside of the column. It is equivalent to the fraction of δ-electrons which receive an energy greater than E_0, which is needed to leave the ionization column. F can therefore be written as

$$F = \left(\frac{dE}{dx}\right)_{E>E_0} \bigg/ \left(\frac{dE}{dx}\right) = \frac{1}{2} \cdot \frac{\ln\left(2E_e\beta^2/I\right)}{\ln\left(2E_e\beta^2/E_0\right)},$$ (3.11)

where the appropriate stopping power formula has to be inserted. For reasons of simplicity, the non-relativistic Bethe-Bloch formula was used here in the first order Born-approximation. Using the Bethe-Bloch formula again and rearranging the terms to $\beta^2 \sim z^2 \left(\frac{dE}{dx}\right)^{-1}$, one observes that F introduces an explicit dependance on the particle charge z, a feature which was neither included in (3.4) nor in (3.7). A charge dependance was found experimentally by Voltz et al. [50] and other authors [51].

Equation (3.10) is much more complicated to handle than the other two, but can be simplified for many practical purposes. In the case of incident electrons the formula assumes a particularly simple form. Electrons of energy E may only transfer a maximum of $\frac{1}{2}E$ to secondary electrons because of their indistinguishability[6]. It is assumed in the analysis of the data of this work that high energy

---

[5]At the end of the path of a δ-electron, the high dE/dx creates a locally high concentration of ionizations. Such a zone may be treated like the interior of the ionization column. The fast δ-electrons thus contribute with a quenched and an unquenched part. However, in the mathematical description, the quenched part may be merged with the term describing quenching within the column, so this only modifies the parameters $A_s^{(1)}$ and $A_s^{(2)}$.

[6]The electron which possesses the greater amount of energy after the collision is *by definition* the primary electron. In consequence an electron may only transfer half of its energy. Other particles do not show this behavior.

δ-electrons which could escape the ionization column are much less numerous than electrons which contribute to the ionization density within the column. This is equivalent to $F = 0$ and the linear part in (3.10) vanishes. If the contribution of the triplet states may also be neglected, the equation reduces to (3.9). The validity of the above assumption is discussed in chapter 6.

Chapter 4

Experimental setup to determine the scintillator response

4.1 Motivation

In the Double Chooz experiment the neutrino energy in a given event is reconstructed from the scintillation light intensity. The positron from the inverse β-decay (1.2) carries the information about the kinetic energy of the neutrino and this energy information is used to identify candidates for neutrino related events and separate them from background. The 8 MeV energy from the Gd(n,γ)-reaction also has to be reconstructed precisely in order to know the error of the energy cuts. However, as elaborated in the previous chapter, the response function $L(E)$ is non-linear for low particle energies. At a first glance it may look like the exact low-energy behavior was not particularly relevant for the experiment, for all neutrino-related events have an energy of at least 1 MeV (from the positron annihilation). Furthermore the lowest detector trigger threshold is set at 0.5 MeV [20]. But the processes described in section 3.4 deal with charged particles, whereas in the experiment both positron and neutron produce uncharged photons. They first have to create electrons through the Compton effect and the energy spectrum of the Compton electrons is broad. In fact, from the Klein-Nishina formula

$$\frac{d\sigma}{d\Omega} = \frac{e^2}{2\,m_e^2 c^4} f(E_\gamma, \phi)^2 \left[f(E_\gamma, \phi) + f(E_\gamma, \phi)^{-1} - \sin^2(\phi) \right], \qquad (4.1)$$

with $f(E_\gamma, \phi)$ being the ratio of electron energies after and before the scattering (see (4.2)), follows that for sufficiently energetic photons scattering angles ϕ of around zero are the most probable [52]. A high-energy gamma is therefore likely to produce several low-energy electrons, which then individually produce scintillation light, each affected by ionization quenching. The scintillations of the numerous Compton-electrons then sum up to the total light yield, attributed to the original gamma ray.

A detailed knowledge of the response function $L(E)$ is therefore indispensible for an accurate energy reconstruction. In particular, the quenching model and parameters implemented in the Geant4-based Double Chooz simulation software have to be adjusted so that they succeed to reproduce the light yield as well as possible. The response of the Double Chooz scintillator liquids to low-energetic electrons was investigated at the Max-Planck-Institut für Kernphysik in the context of this diploma thesis.

4.2   Concept

The scintillator response function $L(E)$ is linear for higher energies, so the focus of interest lies on the scintillation light yield in response to incident low energy electrons. The overall strategy to obtain the light yield curve is to measure the sample's light output for a number of defined electron energies. The challenge in such a straight-forward approach is that there are no suitable monoenergetic electron sources.

The use of an accelerator device would be an option, but requires a considerable amount of space and money. An important disadvantage for the experiment itself is that irradiation by externally accelerated electrons is connected with surface effects. The light output of the scintillator is reduced if the ionizing particle has only a short residual range within the liquid. The reason for this is that energy migration takes place isotropically and excitation energy near the surface can "leave" the scintillator without being captured. Although the surface quenching can be satisfyingly parametrized [28], this would introduce new quantities to handle and new sources of possible errors. Techniques like velocity selection and other modern methods to create monoenergetic electrons also manipulate an external electron beam and are prone to surface effects. To avoid this, one can try to create monoenergetic electrons directly within the sample. Auger emitters produce monoenergetic electrons, but their creation is connected with the emission of X-rays when the electrons rearrange afterwards. Furthermore, one could only test those electron energies for which an emitter exists - which are mostly energies that are too small for this purpose.

The method used in this work employs Compton scattering of gamma rays. In this concept, gamma rays from a radioactive source scatter off an electron in the liquid scintillator sample, which takes away the energy lost by the photon and creates light. A photomultiplier tube (PMT) observes the sample's light output. The photon and electron energies E'_γ and E_e after scattering are connected by
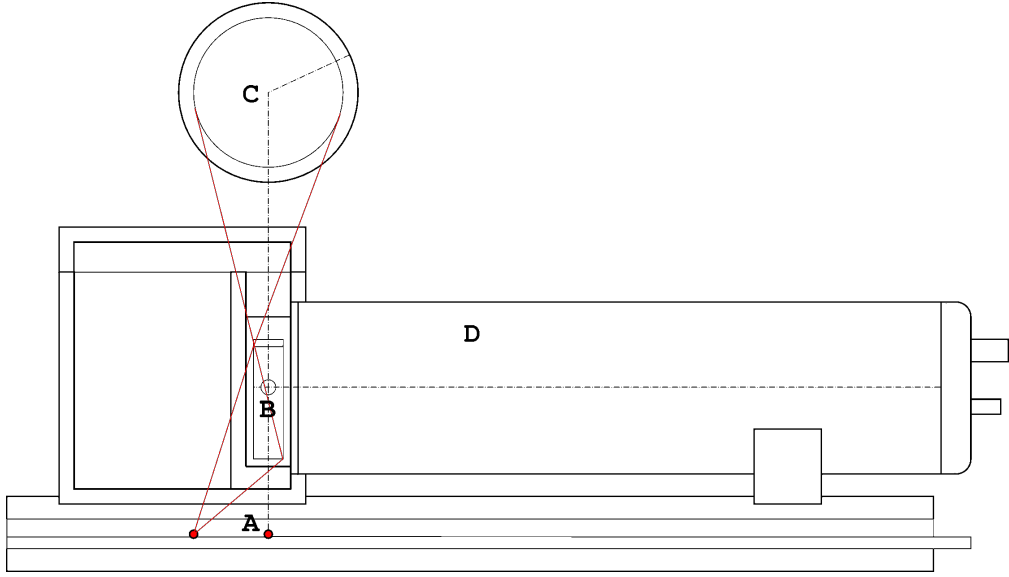
Figure 4.1: Schematic view of the experimental setup. Main parts are the ^{137}Cs sources (A), the scintillator cell (B), the germanium spectrometer (C) and the PMT (D). The smallest and largest scattering angle possible for the second source are also drawn. The schematic is not true to scale.

the Compton formula

$$E'_\gamma = \frac{E_\gamma}{1 + \frac{E_\gamma}{m_e c^2}\left(1 - \cos\phi\right)} = E_\gamma f(E_\gamma, \phi), \tag{4.2}$$

$$E_e = E_\gamma - E'_\gamma, \tag{4.3}$$

where ϕ is the angle in which the photon is scattered and E_γ is the initial photon energy. If the gamma rays come from a monochromatic radioactive source, E_γ is known from the decay energy. But still, the photons can take any scattering angle and the electron energy spectrum is broad. Rather than to utilize monoenergetic electrons, the electron energy E_e is reconstructed and related to a specific scintillation signal with the help of a coincidence circuit. In an adequate configuration it can be assumed that when a PMT pulse coincides with a signal from a photon detector, these events come from the same photon.

E_e is reconstructed from the photon energy E'_γ via (4.3). There are two possibilities to get E'_γ. It can either be obtained from the scattering angle ϕ or measured directly. We opted for a direct energy measurement using a high-resolution germanium spectrometer. This method was considered superior due to the very high energy resolution of the Ge-detector. E'_γ can be measured precisely in a compact setup and with a high counting rate. To achieve a similar precision with a measurement of ϕ, a large distance between source and sample is required. This makes the apparatus unwieldy and, since the number of registered photons decreases by $1/r^2$, drastically reduces statistics. Depending on the source activity,

this may lead to significantly longer measurement times. Additionally, such a setup would be sensitive to slight changes in the geometry, which is a possible source of errors.

4.3 Experimental setup

The setup used was based on a configuration by Ch. Aberle. I enhanced it for the ionization quenching measurements and tested it for systematics. It is illustrated schematically in fig. 4.1. Central component is a glass cell of 10 mm × 10 mm × 35 mm inner dimensions, containing the scintillator mixture to be measured. For light protection, it is stored in a light-tight blackbox. The sample is irradiated by gamma rays from two point-like radioactive sources below the vial. The γ-emitters in use are ^{137}Cs sources of ca. 400 kBq and 200 kBq activity, which emit only monoenergetic photons of 662 keV energy. A Photonis XP2262 photomultiplier tube is tightly mounted to a circular window in the box and optically coupled to the vial (see section 5.3). It observes the scintillation pulses created when a Compton electron is stopped in the scintillator and produces light. The PMT is operated in the proportionality region at a voltage of 1620 V so that the PMT charge signal is proportional to the light intensity (see section 5.4). The germanium spectrometer utilized is a detector produced by PGT with a relative efficiency of 31 % and a resolution of 2.3 keV FWHM at 1.33 MeV photon energy specified by the manufacturer. The sensitive germanium mono-crystal of the photon spectrometer resides in an aluminum cylinder and is placed directly above the sample. The operating voltage was raised to 3.375 kV, where the leakage current remained on a low level. At this voltage the detector yields voltage pulses that are proportional in height to E'_γ (see section 5.1). The important events are those in which a photon from the source undergoes Compton scattering in the sample and is deflected into the direction of the Ge-spectrometer where it is detected. These events are selected in the coincidence unit, where the coincidence of a Ge-pulse and a PMT-pulse is required.

Only events in which the photon hits the Ge-detector after scattering are selected (background events are discussed in section 4.4.1). In our geometrical configuration this is only possible for small scattering angles. In this way we achieve to select Compton electrons of the desired low kinetic energy. The 200 kBq source directly below the cell allows angles ϕ_1 between 0° and about 20°, corresponding to E_e up to 50 keV. To collect data points for higher energies as well, the second ^{137}Cs source activity was placed in 1.5 cm horizontal distance from the first source. The larger scattering angles ϕ_2 correspond to about 30-160 keV electron energies. Apart from the selection of the energy range, the apparatus is not sensitive to changes in the geometrical configuration.
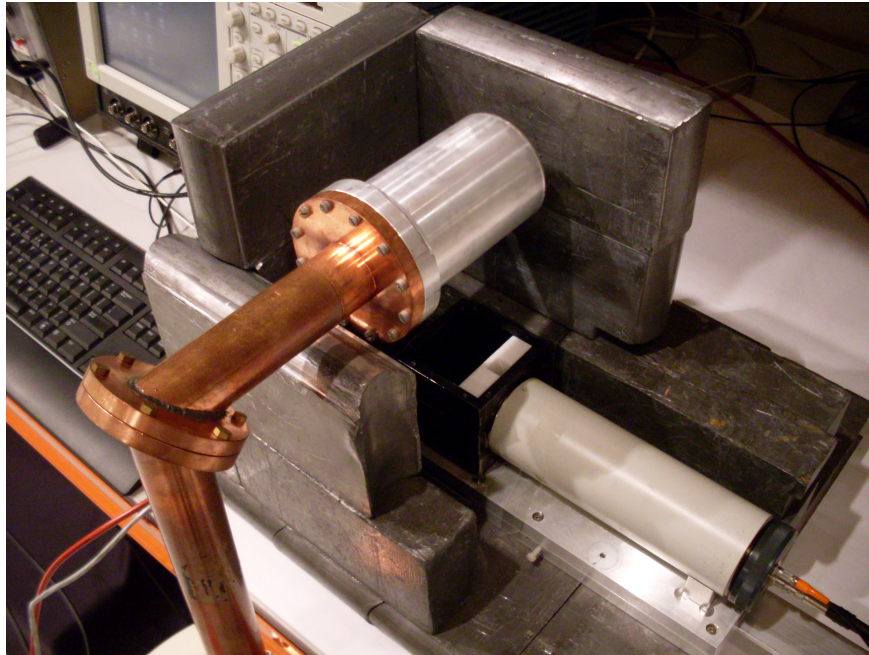
Figure 4.2: Photograph of the experimental setup. The germanium crystal is mounted within the aluminum cylinder, the PMT and the open blackbox are seen below. The white sample holder with the cut-out for the sample is visible inside the box. Lead shielding and light protection have been removed for demonstrational purposes. The radioactive sources are placed below the blackbox and cannot be seen on the photo.

To minimize background radiation, the experiment is conducted at the low-level laboratory at the Max-Planck-Institut für Kernphysik. It is located underground and has an overburden of 15 m w.e. The whole setup is further shielded from radiation by lead blocks. For additional light protection the PMT and the blackbox with the sample are wrapped up in a black, rough-textured cloth. The complete setup in real life is shown in fig. 4.2.

Sample preparation

The samples studied can be found in section 6.1. All liquid samples are measured in a rectangular glass cell. Before a liquid scintillator is filled into the vial, it is thoroughly cleaned with cyclohexane. It is then left in an oven at $> 100\,°C$ for cyclohexane residues to evaporate. After cooling it is purged with some drops of the scintillator sample and then finally filled.

As the liquid is exposed to air during the loading process, it is purged with nitrogen to remove dissolved oxygen (see section 5.2). The cell is then instantly plugged with a teflon cap and sealed with a teflon strip. Further proofing was achieved with a special putty which is used for vacuum applications. To avoid

contact of the putty with the coupling oil, a second layer of teflon is put around the vial cap.

Electronics
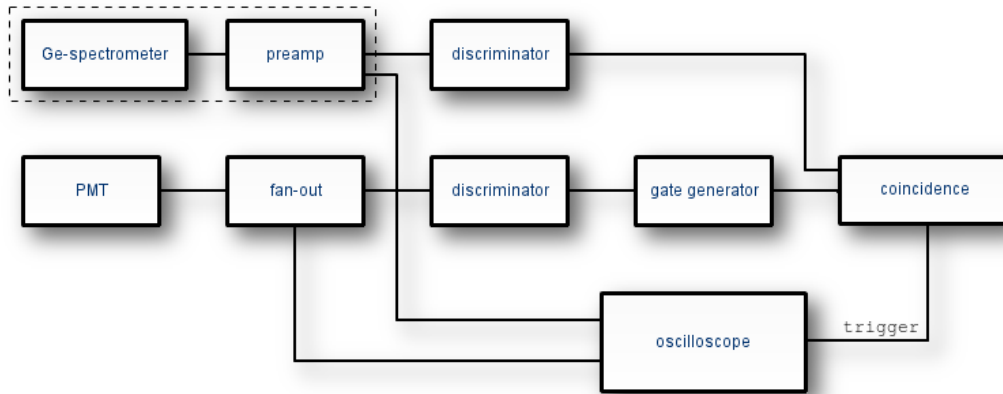
Figure 4.3: Scheme of the electronic circuitry used in the experiment.

A schematic view of the circuitry is given in fig. 4.3. The PMT- and Ge-signals are wired through several NIM-modules and create the trigger signal if the coincidence condition is fulfilled. The coincidence unit is a LeCroy 465 module. The Tektronix TDS 7054 DPO oscilloscope records pulses in a time range of 4 μs and writes the complete pulse forms into a file when a trigger is released[1]. It has a resolution of 10000 channels on the time axis and 256 channels on the voltage axis. The scale set is 1000 mV for the Ge-pulses and 2000 mV for the PMT-pulses.

Photon energy and scintillator light output are determined from the pulse forms (fig. 4.4). The information about the light intensity L is contained in the electrical charge created in the PMT. The output voltage can be assumed proportional to the PMT current as given by Ohm's law, so the total charge is proportional to the pulseform integral over time. The PMT signal is integrated offline in the analysis program. The γ-spectrometer uses a preamplifier and its output signal is already integrated. Its charge information is in the pulse maximum.

Both signals are needed in duplicate: one to create the coincidence, the other for the oscilloscope. The spectrometer preamp already provides two output channels of which one directly enters the oscilloscope and the other the coincidence circuit. The PMT only offers a single output, so the signal has to be split in a

---

[1]A separate file for each input channel is created.

(a) Ge-signal

(b) PMT-signal
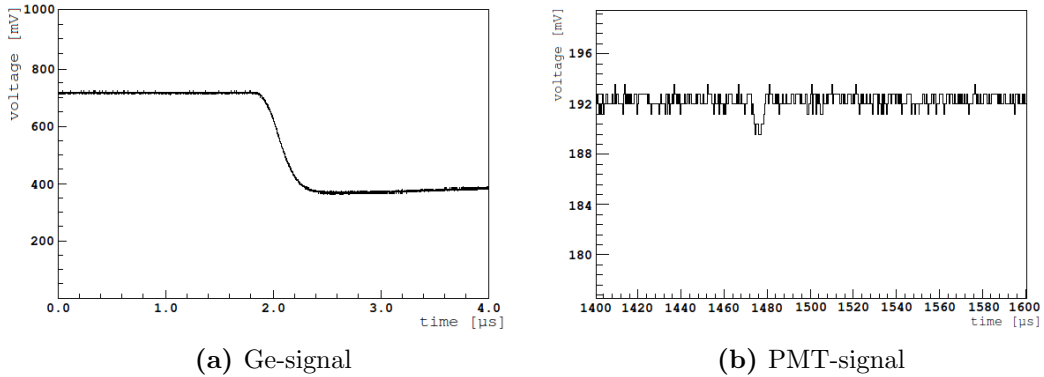
Figure 4.4: Typical signals of the germanium detector (a) and the PMT (b) for a scintillation event caused by a low-energy Compton electron. The abscissa shows the time after the oscilloscope started recording, the ordinate displays the voltage. The Ge-spectrometer yields a large pulse due to the high energy of the scattered photon, while the electron only creates a small PMT signal.

fan-out gate. A LeCroy 428F fan-in/fan-out module is used for this task. Again, one of the outputs is used for the oscilloscope and the other for the coincidence electronics. More details on this can be found in 5.4.1.

The signals used for the coincidence first run through a PS 730 discriminator module and are converted into logical pulses. For the PMT signal a careful choice of the discriminator threshold is important. As we are mainly interested in scintillations from low-energy events, the threshold has to be low enough to let the associated small voltage pulses pass. On the other hand it has to filter out the *dark noise* coming from single photon events. The dark pulses have a frequency in the kHz range. The threshold was lifted until the event rate dropped significantly below this value. Together with a reasonable safety margin the threshold was set to 11 mV above the baseline position. The Ge-signal is not affected in such a way, for the high pulses belong to high E'_γ and small E_e in the scintillator. Consequently, a high threshold of 230 mV above the baseline was chosen.

Before the logical pulses produce the coincidence, the (logical) PMT signal is fed into a Ortec 416A gate generator. The germanium signal passes the preamplifier and has a longer rise time than the fast PMT pulse. Therefore the PMT pulse arrives earlier and opens the gate. An additional delay is not necessary and the adjustable delay is held on its minimum of 0.1 μs. The gate width is equivalent to the coincidence time T_{coinc}. Correlated logical pulses from the PMT and the germanium spectrometer are proximate in time. The distribution of their time distance has been analyzed to adjust the coincidence time. It has been

32

found that most Ge-signals that can be related to a clean coincidence follow the PMT-start signal within 500 ns, which has been chosen as T_{coinc}.

4.4   Analysis of the pulse data

The oscilloscope registers complete pulseforms and upon a trigger writes them into a separate file for each channel. Each event consists of ten thousand 8-bit data points, preceded by a 7 byte long header and followed by a single line break control character. The file is in ASCII format and consecutive events are successively appended to the end.

Each data file contains more than one million pulseforms and their evaluation is automatized. For that purpose a program was written. It is based on a `Fortran` code written by St. Schönert and modified by Ch. Aberle for light yield and timing measurements of the Double Chooz scintillators. I extended the program for the quenching measurement and ported the code to `C++` for usage with the data analysis framework `Root`. It creates `Root`-histograms which are then further processed in the following steps of the analysis procedure. The program has been extensively tested to ensure the reliability of the program output. It has to calculate the integral over the PMT pulse to get the charge and search for the Ge-pulse maximum for E'_γ. In addition, the analysis program has to reject defective events and various algorithms have been implemented to sort them out.

4.4.1   Program structure

The program flow is depicted in the flowchart in fig. 4.5. After initialization, the pulses from the two data files are read. The first cut is already applied at this stage: if the pulse reaches the limit of the oscilloscope voltage scale it was probably cut in height and is filtered out. The analysis starts with an estimation of the baseline position. The mean value μ_{b} and the standard deviation σ_{b} are calculated over 1.12 μs. This is done separately for every pulse as this makes the analysis indifferent to fluctuations in the baseline offset.

Then the pulse onset is determined. When a number of consecutive channels are farther away from the baseline than a certain given threshold (2 channels for the PMT and 1.5 channels for the Ge-detector), the pulse is considered to start there. If this condition is not fulfilled within a pulse signature, then no pulse is found and the event is rejected. When the onset position is known, a refined value of μ_{b} and σ_{b} is calculated where a certain range of channels before the onset are taken into account. If the new σ_{b} is too high, this may indicate *jitters* or piled-up signals, and the corresponding events are hence rejected.

The previous steps are common for PMT and Ge-pulses. The further treatment is different. The PMT pulse is numerically integrated with the baseline taken as the zero line. The integration width is 140 ns, which spans over the en-
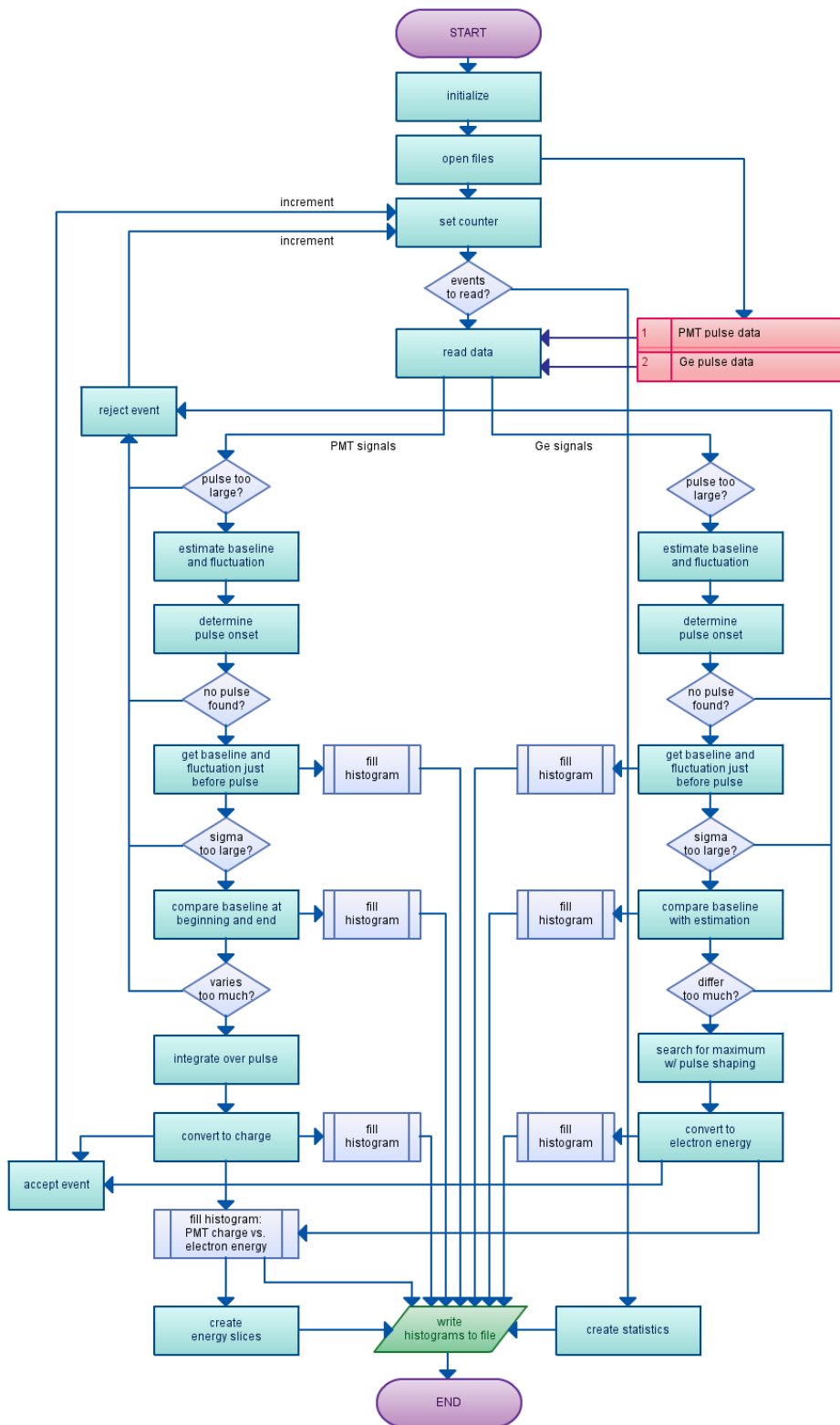
Figure 4.5: Structure of the analysis program.

tire pulse. From the integral the PMT charge is computed. In the Ge-signal the algorithm searches for the pulse maximum. To limit the effect of small voltage fluctuations, a simple form of pulse shaping is applied. Instead of just looking for the highest channel, the mean value over n consecutive channels is taken. Then the difference from the baseline to the highest mean value is considered the pulse height. This method is possible because the Ge-signals change slowly at this time scale and there are enough channels to calculate an unbiased mean value. A window width of $n = 70$ has proven to give accurate results. The pulse height is then converted into the electron energy by utilizing the results of the calibration measurements (see section 5.1) together with equation (4.3). Then the sequence is repeated for the next pair of pulses.
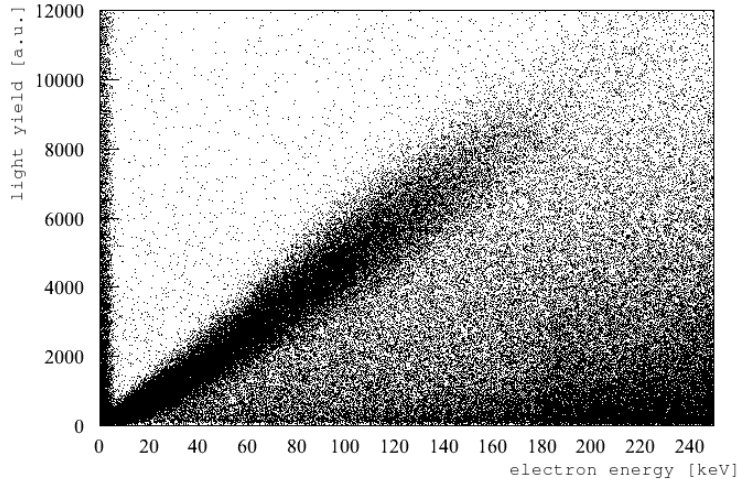
Figure 4.6: The distribution of obtained light yields vs. the electron energy deposited in the scintillator. The dense cloud of events cointains the response curve. The other points are background. The events on the left margin are accidental coincidences where a gamma ray directly hits the spectrometer, while another one creates light in the cell.

Throughout the process several histograms are created. They are filled with information from accepted pulses. The most important one is the two-dimensional distribution of the light intensity L in relation to the electron energy. A typical diagram is shown in fig. 4.6. In principle, this scatter plot already contains the scintillator response curve $L(E)$ as the dense cloud of events which extends diagonally over the diagram. But as electrons of a certain energy produce light intensities in an approximate Gaussian distribution, the response curve is "smeared out". To get the pure $L(E)$ curve back, the histogram is *sliced*, i.e. for separate narrow intervals $[E_1, E_2]$ of the electron energy the light yield distribution of events lying within this interval is projected into a new histogram

(fig. 4.7). An energy slice can be represented by a vertical cross section of the distribution fig. 4.6 at a certain electron energy. A slice width of 2 keV has been chosen, considering that the energy resolution of the Ge-spectrometer is of that magnitude (section 5.1). The electron energy attributed to the slice is the mean energy of the events within the slice, which is also computed directly by the program. For simplicity, the slices are labelled with their approximate mean energies[2]. The further analysis procedure is explained in the following section.

The other histograms produced are primarily used for systematic studies and to determine the cut parameters of the program. After the first execution, the cut parameters are obtained from these histograms and adjusted in the source code. The program is then repeatedly executed until the cuts filter out defective events effectively while accepting the good events. 100 pulses are observed manually to check that the analysis program performs well.

Types of accidental coincidences

Typically, about 40 % of the events recorded are not related to a clean coincidence. But many of the accidental coincidences can be identified and rejected in the analysis. The most common cause of accidentals are triggers on the slowly decaying flank of the germanium signal. The decay time of the Ge-pulse is of the order of 100 μs, so the flank can be regarded constant on the timescale of a PMT pulse, as seen in fig. 4.4. When it falls just below the trigger threshold, only a slight fluctuation in the signal suffices to pass the threshold again and cause another logical signal, which - together with a preceding PMT pulse - can fake a coincidence. As the germanium signal height is calculated in relation to its baseline, the program does not find a pulse and rejects the event.

Another class of undesired events are those where the scattered photon does not deposit its total energy in the germanium crystal - or inversely, a photon is scattered into the spectrometer from a place other than the scintillator. In this case the energy of the electron in the scintillator is overestimated. As both pulses themselves do no not show any irregularities, they cannot be sorted out by the program and fig. 4.6 is populated with points under the diagonal cloud. They can however be identified as background in the slice histograms (see section 4.4.2).

Many gamma rays deposit a part of their energy in the surrounding lead blocks and cause secondary X-ray emissions from lead atoms, which can hit the spectrometer. If they hit the spectrometer, they also fake a high-energy electron (> 600 keV) in the scintillator. These events cause two dense lines, which lie beyond the range of fig. 4.6 and cannot be seen. Events, where a photon first hits the detector and is backscattered into the scintillator cell, are correlated events. For each of the two sources they can happen within a narrow range of

---

[2]for example "20 keV-slice" instead of "19.987 keV-slice"

angles. They therefore lead to two denser areas to the right of the diagram. Neither of these two sorts of accidentals can be detected by the software. On the other hand, they do create false events in an energy range that is beyond the region of interest (see section 4.4.2).

4.4.2 Obtaining the response function

The light yield curve can be obtained from fig. 4.6; it is the locus of highest point density in the bulk of events. In order to get a clean curve, all slices are fitted to get a light yield value associated with the mean electron energy of the respective slice. An exemplary energy slice is given in fig. 4.7. The events in the left part of the spectrum are background events. They are modelled by an exponential function. The information about the scintillator response is contained in the peak to the right. Its exact form and the function used for fitting are discussed in the following.

Photocurrent distribution

The details of the photomultiplier tube have not yet been addressed in this document. For very low light intensities, as they are measured here, the details of the photodetection mechanism are of importance. In this case the quantum nature of light comes into play.

A photon hitting the photocathode creates a primary photoelectron (PE) with a certain probability ϵ. The core component of a PMT is the cascade of
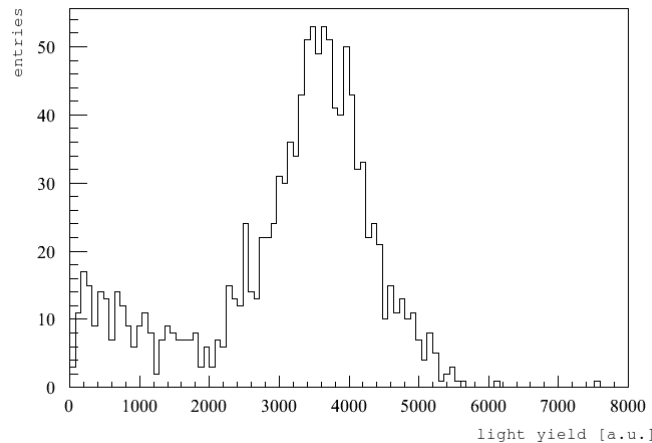
Figure 4.7: Energy slice of ca. 60 keV mean electron energy. The entries to the left are background. The mean value of the peak is the light yield response to electrons of that energy.

37

dynodes, with a high potential difference lying between them. A primary PE is accelerated in the strong electric field and gains kinetic energy. When it impacts on the dynode material, it releases numerous secondary electrons which in turn are accelerated towards the next dynode. The cascade thus leads to an avalanche effect so that in the end a measurable current is produced. The total number of electrons released is normally distributed. If more than one photon hits the photocathode within a short time, several primary PEs may be created. The number of electrons in the PMT output current is then the sum of the numbers of secondary electrons released by all the PE. The total charge in a PMT pulse therefore scales with the number of incident photons.

While the PMT charge (proportional to the number of secondary electrons) per PE is normally distributed, the number of PEs produced in an individual scintillation process (of N photons hitting the photocathode) is not. Of the incident photons, only a fraction is detected due to the PMT efficiency ϵ. So the number of PEs is small in a certain range of light intensities and therefore follows a Poisson distribution rather than a Gaussian. The complete distribution of the PMT output current for a specific number of incident photons now composes of the discrete Poissonian distribution of the PEs, and for every possible number of PEs the continuous Gaussian distribution of the output charge.

$$\mathcal{I}(A_0, \lambda, \mu_n, \sigma_n; \, x) = A_0 \sum_{n=1}^{N} \mathcal{P}(\lambda; \, n) \, \mathcal{N}(\mu_n, \sigma_n; \, x), \qquad (4.4)$$

where

$$\mathcal{P}(\lambda; \, n) = \frac{\lambda^n e^{-\lambda}}{n!}$$

$$\mathcal{N}(\mu_n, \sigma_n; \, x) = \frac{1}{\sigma_n \sqrt{2\pi}} \exp\left(-\frac{(x - \mu_n)^2}{2\sigma_n^2}\right).$$

with λ being the mean value of the Poissonian distribution and μ_n and σ_n the mean values and standard deviations of the respective Gaussian functions. A_0 is an overall scaling factor. The Poisson term gives the general photoelectron distribution, the Gaussian then takes these values as its amplitude and "smears" the corresponding output charge signal. The total distribution is then the superposition of these. This function would require two fit parameters μ_n and σ_n for each term considered plus the parameters A_0 and λ. But one can exploit a relation between the different parameters for n. Assuming that each PE has the same charge distribution, the distribution of n primary PEs is the convolution of n independent and identically distributed Gaussians $\mathcal{N}(\mu, \sigma; \, x)$, which yields $\mathcal{N}(n\mu, \sqrt{n}\sigma; \, x)$. Secondly, the positions of the mean values μ_n are equidistant and can be replaced by ns, where s is a scaling parameter.

$$\mathcal{I}(A_0, \lambda, s, \sigma_0; \, x) = A_0 \sum_{n=1}^{N} \mathcal{P}(\lambda; \, n) \, \mathcal{N}(s \, n, \sigma_0 \sqrt{n}; \, x) \qquad (4.5)$$

This distribution only processes the four parameters A_0, λ, s and σ_0, independently of the number of terms. Still, the large number of summands make (4.5) difficult to handle as an effective fit function. Although for a practical treatment one only has to consider terms within the approximate range $n \in [\frac{1}{2}\lambda, \frac{3}{2}\lambda]$, a light pulse with $\lambda = 50$, which is a realistic value for electron energies around 20 keV, would already require 50 summands in (4.5).
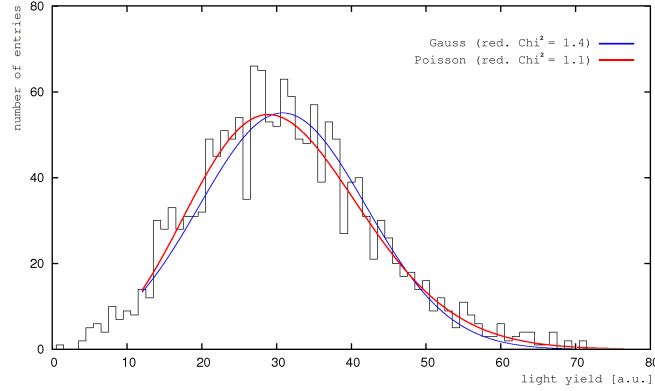

Figure 4.8: Gaussian (blue) and "Poissonian" (red) fits to a 19 keV-slice. In this particular slice the Gaussian mean is $\mu = 30.8$. The Poissonian yields a men number of PEs $\lambda = 14.8$, which converts with the scaling parameter $s = 0.478$ PE/channel to a mean light lield of 30.9 on the same scale. This is a difference of 0.3 %. It is worth noting that the mean value and the maximum of the detailed function do not coincide. The χ^2-value of the Poissonian indicates a better fit to the curve, but the exact form of the fit curve is irrelevant in the context of this experiment.
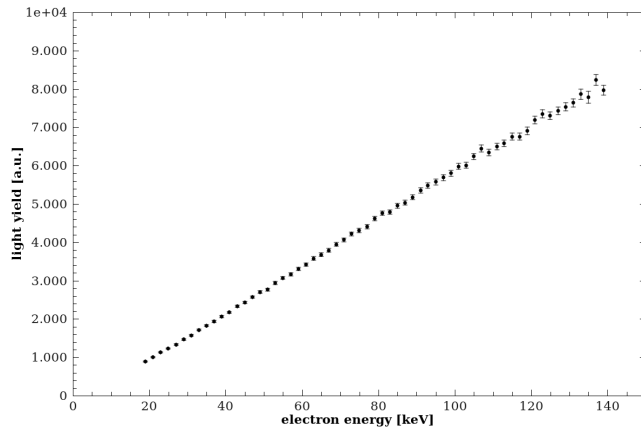
Figure 4.9: Light yield data points obtained after the slice fitting procedure.

39

However, the interest does not lie on a good fit to the data itself but on the position of the mean value. It was tested if a normal distribution fitted to the data would yield a similar mean value as (4.5). For very large numbers of photons this approximation would obviously be valid, but the situation is not clear for the relatively small numbers of photons dealt with here. Both fits were applied to the low-energy slices and both gave nearly identical results for the mean value (fig. 4.8). It was concluded that a normal distribution is well suited to determine λ, as the accordance between the two curves even rises with larger number of photons.

The slices were fitted one after the other in `Root`. The fit function used was the sum of a exponential and a Gaussian function. The leftmost part of the spectrum was not included in the fit range to avoid effects of the discriminator threshold. The mean value μ and its uncertainty were obtained directly from `Minuit` and plotted against the electron energy in the slice. An illustrative plot of the response function is given in fig. 4.9. The results for the Double Chooz scintillators are discussed in chapter 6.

Chapter 5

Study of systematics

5.1 Germanium detector calibration

The energy of the scattered photon E'_γ is measured in a germanium spectrometer. If a photon interacts within the mono-crystal, it has a high probability to deposit its total energy via photoeffect. Photons that undergo Compton scattering and only deposit a fraction of their energy in the detector crystal contribute to background.

The spectrometer has a built-in preamplifier. The preamp circuit also works as an integrator, so that the energy information is converted into the height of the output voltage pulse. To reconstruct E'_γ from the pulse heights, the spectrometer
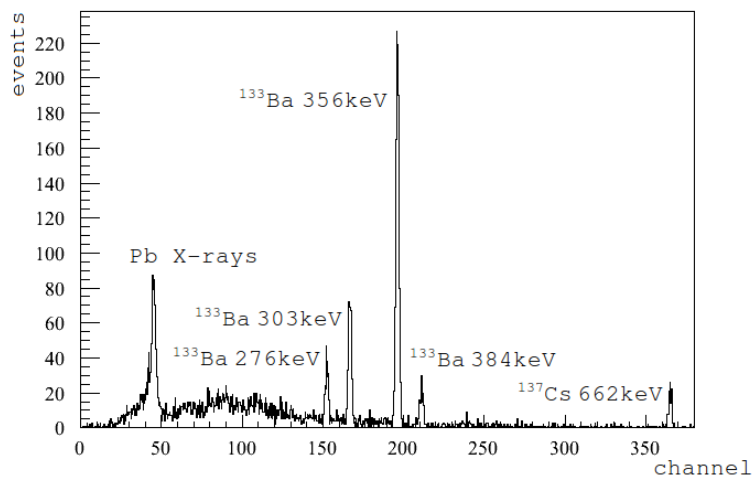
Figure 5.1: Typical calibration spectrum obtained with the sources ^{133}Ba and ^{137}Cs. The number of events is plotted against the detector signal height (in oscilloscope channels).

Source	Energy	μ_{Ge} [channels]	σ_{Ge} [channels]	Fwhm [keV]
^{137}Cs	661.657 keV	365.03 ± 0.10	0.93 ± 0.07	4.0 ± 0.3
^{133}Ba	383.848 keV	211.10 ± 0.09	0.99 ± 0.07	4.2 ± 0.3
^{133}Ba	356.013 keV	196.08 ± 0.03	0.93 ± 0.02	4.0 ± 0.1
^{133}Ba	302.851 keV	166.81 ± 0.05	0.92 ± 0.04	3.9 ± 0.2
^{133}Ba	276.400 keV	152.32 ± 0.09	0.74 ± 0.06	3.2 ± 0.3

resulting slope: 1.8103 ± 0.0027 [keV/channel]
resulting offset: 1.02 ± 0.63 [keV]

Table 5.1: Exemplary results of a calibration measurement before one run. The values extracted for slope and offset of other calibration curves differ only slightly of those given here.

has to be calibrated. The detector is calibrated separately for each measurement. To make sure that the calibration parameters do not change during the measurement, the γ-spectrometer is recalibrated before and after each run.
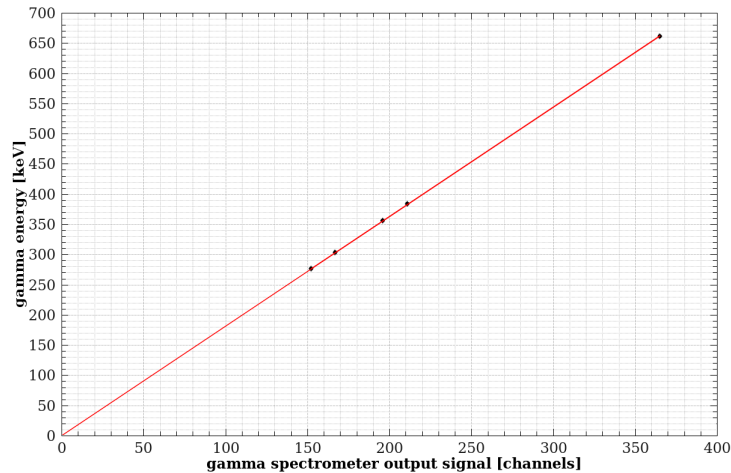
Figure 5.2: Linear fit to the calibration data points.

The monoenergetic ^{137}Cs source of 662 keV and a ^{133}Ba source serve as a benchmark. ^{133}Ba provides four strong lines of 276 keV, 303 keV, 356 keV and 384 keV. To obtain the energy spectrum 10000 events are recorded. A typical spectrum is given in fig. 5.1. The five peaks from cesium and barium can clearly be seen and identified with the energies given above. The bulk on the left are X-rays from the lead screening. The lines observed are the K_α and K_β lines. In
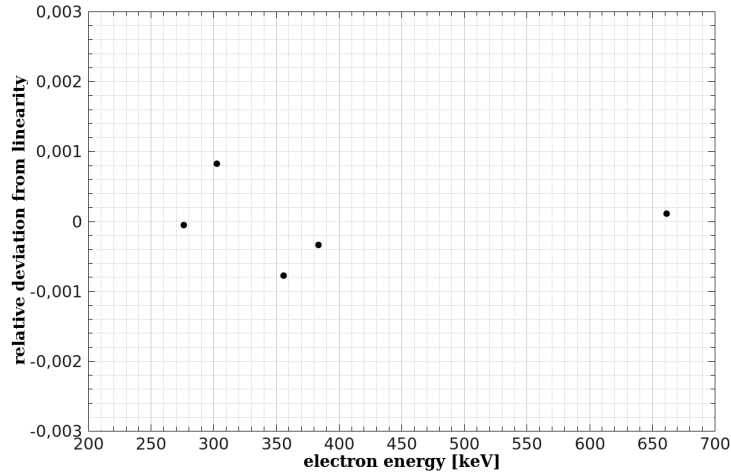
Figure 5.3: Relative deviation of the germanium detector signal from linearity.

principle they could also be used for calibration, but the lines are very close and cannot be clearly separated with this relatively little number of events. They are therefore not used for calibration. Typical calibration results are compiled in table 5.1. A linear fit is then applied to the data points (fig. 5.2). The slope and offset obtained define the calibration curve.

The linear behavior of the γ-spectrometer's output pulse heights with E'_γ was confirmed in our measurements (fig. 5.2). The detector resolution can be obtained from the peak widths. The standard deviations are smaller than one oscilloscope channel, which after conversion gives an energy resolution better than 2 keV. This also defined the size of an energy slice, which was set to 2 keV. The FWHM are around 4 keV (table 5.1). That this is not as good as the specification is due to the resolution of the oscilloscope limited to 8 bit on the voltage scale. The two calibration curves before and after a measurement are then compared. They were always in very good concordance with each other and agreed within the uncertainties. In the analysis of the Compton coincidence experiment the mean values of the two calibration measurements - weighted by their uncertainties - are used to calculate E_e.

The relative deviation from linearity of the Ge-signal is smaller than 0.1 % (fig. 5.3) and was neglected in the analysis. An effect of the sizes chosen for the slices was also not considered.

5.2 Nitrogen purging and light yield stability

A disadvantage of liquid scintillators compared to plastic or crystal scintillators is their sensitivity to oxygen. Contact of the liquid with air instantly results

in oxygen molecules dissolving in the mixture and even small amounts can considerably reduce the light yield. The intensity of oxygen quenching primarily depends on the solvent-solute transfer efficiency. Thus the total strength of the effect decreases with increasing fluor concentrations (see section 3.2). Oxygen can also absorb the fluor emission. This effect is more important at higher fluor concentrations. [28]. Due to its reactivity, oxygen often has the ability to form non-scintillating compounds. This effect is irreversible and referred to as *static quenching*.

Oxygen quenching can be described by the Stern-Volmer equation. It relates the light yield of a fluorescent compound to the concentration c_q of a chemical quench agent.

$$\frac{F_0}{F} = 1 + \tau_0 \gamma k \, c_q$$

F and F_0 are the fluorescence intensities in presence and absence of the quencher, τ_0 is the mean lifetime of the fluor excitation without any quencher, k is the interaction rate between fluor and quenching molecules, and γ is the probability that an interaction results in quenching [53]. The concentration of oxygen in a liquid is mainly determined by its partial pressure in the atmosphere over the liquid. According to Henry's law the concentration of a gas in a liquid is directly proportional to the partial pressure, $c_{\text{gas}} = k_{\text{H}} \, p_{\text{gas}}$, for constant temperature. The constant k_{H} is a material constant depending on the gas.

A common method to eliminate oxygen from a liquid scintillator sample is purging with an inert gas like nitrogen or argon. This technique is also utilized in our sample preparation. Nitrogen is discharged into the liquid by a fine nozzle. The partial pressure p_{O_2} of oxygen is zero within the nitrogen bubbles. At the surface, oxygen molecules tend to exit the liquid to increase p_{O_2} in the bubble. The bubble rises to the surface and conveys the O_2 molecules out of the sample. Our vials possess a little neck above the liquid level, where the bubbles push each other towards the upper end, effectively creating a nitrogen atmosphere over the scintillator and protecting it from further contact with air. Furthermore, O_2 molecules can diffuse from the liquid into the nitrogen blanket. In contrast to oxygen, nitrogen does not contribute to quenching in the samples because of the different optical spectra.

The effect of nitrogen purging is studied with the Gamma Catcher scintillator with 2 g/l PPO. Of the liquid scintillators used in Double Chooz, this mixture is the most sensitive to oxygen exposure. Since it contains only 2 g/l PPO, the oxygen molecules can compete heavily with PPO for the energy transfer. We can assume that the time used for the purging of the GC is also sufficient for the other liquid scintillators. The measurements are undertaken in a setup slightly modified to that described in section 4.3 [24]. In a backscatter arrangement the ^{137}Cs source is placed between the photon detector and the sample, so that a

gamma ray is registered when it scatters in an angle of $\phi \approx 180°$. Under these large angles the energy transferred to the electron does not vary much with ϕ, so that E_e is known (449 keV). The measurement could therefore be conducted with a second PMT observing a NaI-scintillator instead of a γ-spectrometer.

The GC scintillator was mixed freshly in the chemistry lab and left exposed to air for several hours, so that the mixture was saturated with oxygen. It was then separated into different specimen which were purged with nitrogen for different durations and the same gas flow. The light yield of the different samples was then measured in the apparatus. It has shown that 10 minutes of nitrogen purging could increase the light yield by roughly 30 %. On the other hand, 30 minutes of purging did not increase the light yield any further. Hence, it was concluded that 10 minutes is enough time get the sample oxygen-free. In the measurements done to determine the ionization quenching the samples were purged for 10-15 minutes.

Typical measurement times for the final measurement were five to seven days and more than 10^6 events were collected in each run. During this time, a decrease in light yield could be observed. In the analysis procedure the first and last 100000 events of the measurements were analyzed separately for several slices and the mean values obtained were compared. In case of the Gamma Catcher, the decrease was about 1 % of the initial light yield per day. The cause for the decrease has not been finally identified and needs further investigation. The target showed a less pronounced decrease in the light yield, which would be an indication of quenching by oxygen in spite of the care that was taken to avoid it. In the target the energy transfer from PXE to PPO is faster than in the GC, and the oxygen molecules have less time to interrupt the energy transfer processes. However, the study of several slices showed that the decrease equally affects the slices of different energies. Therefore it can be assumed that the effect only broadens the Gaussian distribution of the light yield peaks in the slices and drags the mean value to lower values. As the absolute light yield is not significant in this measurement, the decrease in light yield is not expected to add a significant systematic error to the measurement. Under the assumption that the decrease is independent of the energy, this effect was not considered in the analysis of the data.

5.3   Optical coupling

Inside the blackbox the glass vial is placed in a PTFE sample holder, which matches the vial's dimensions. The teflon provides high reflectivity and collects the scintillation light for detection in the photomultiplier tube. Sample vial and PMT are separated by a circular glass window embedded into the sample box. The PMT is mounted directly to the window. On the other side, the PTFE block presses the vial against the window. The dimensions of the block are such that

the vial is secured firmly in its position. To avoid light losses at the small gaps between vial, window and PMT, oil and optical grease are used to couple the components.

Silicone grease is used to couple the PMT to the window. Its high viscosity makes the coupling very stable and suits the grease for long-term applications. The disadvantage is its tendency to create little bubbles when it is applied to the surfaces. It is tedious to remove the bubbles again. As the vial is replaced about every week, it is coupled to the window with paraffin oil, which is better qualified for more frequent tasks. The very similar refractive indices of the vial's fused quartz, paraffin and the scintillator liquids guarantee only minimal reflections at the boundaries.

The coupling can be reproduced well each time the oil is applied. Still, there is the possibility that slight variations of the coupling could influence the measurement. Fluctuations in the oil quantity or possible remaining bubbles could compromise the light yield. We therefore have to make sure that the details of the optical coupling do not influence the light yield measurement. For this purpose the same scintillator was measured three times. The setup used is the configuration from [24] as described in section 5.2. The study was performed with a mixture of PXE and PPO dissolved at a concentration of 6 g/l. To avoid an interference of oxygen quenching, which also could reduce the light yield over time, the sample was already saturated with oxygen.

For this investigation, the scintillator light yield was measured five times. Between each run the oil was first removed and the coupling then renewed again. The results in this data set showed a variation of 1.1 % in the light yield. A second set of measurements where the coupling was kept intact was then run with the same sample. They showed a variation of 1.7 % between them. It could thus be concluded that an error due to the coupling could not be seen.

To renew the coupling, the lead shielding has to be partially dismantled, the light protection has to be unfolded and the PMT's high voltage has to be shut down. After renewal the arrangement is reassembled and the PMT voltage is powered up again. This measurement therefore also includes the possible influences of slight differences in the arrangement and the PMT's operational voltage. These effects are therefore neglected in the overall systematic error.

5.4 Electronics and PMT linearity

Most of the circuitry is not critical in terms of non-linear effects, since the input signals are converted into logical signals at an early stage of the coincidence setup. Nevertheless, one critical point remains where a possible non-linear behavior of the electronics might kick in: the PMT only has a single output channel and the signal has to be split in order to feed it into the oscilloscope as well as into the

coincidence circuit. The Ge-detector posesses two output channels, of which one directly enters the oscilloscope, so this signal is not influenced by possible non-linearities of electronics. The detector and preamplifier themselves are sufficiently linear (see also section 5.1) and both output channels have been checked to give identical signals. The fan-out and the PMT itself, as well as the oscilloscope have been tested for linearity.

5.4.1 Fan-out linearity

I used a pulse generator to provide the input signals and chose a narrow signal of 4 ns width. Together with the rising and falling flanks of 2.5 ns and a certain smoothing of the edges due to electronics, the pulse resembles a PMT signal. The amplitude can be varied between 50 mV and 5000 mV; the frequency was fixed at 1 ms. This gives the fan-out gate enough time to recreate. The pulser provides separate output channels, of which one directly enters the oscilloscope, while the other is looped through the fan-out before. For each amplitude 1000 events are recorded. The oscilloscope writes down the original signals as well as the looped-through signals.

As the fan-out is used for the PMT only, it is of interest if the gate reproduces the pulse integral, rather than the pulse height. For the analysis, the signals coming from the pulser and fan-out were integrated. The pulse integrals showed a narrow normal distribution, which was fitted with a Gaussian function to obtain the mean value. The fan-out mean values were then plotted against the pulser means (fig. 5.4). Within the region of interest the deviation from linearity is 0.4 % (fig. 5.5).
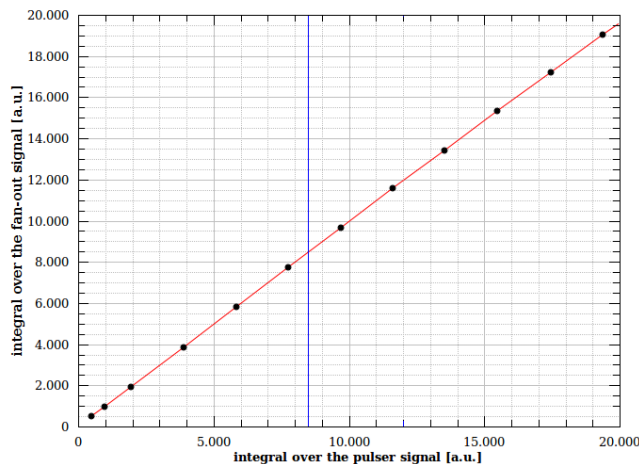
Figure 5.4: Pulse integral from the fan-out versus the integral from the pulser.
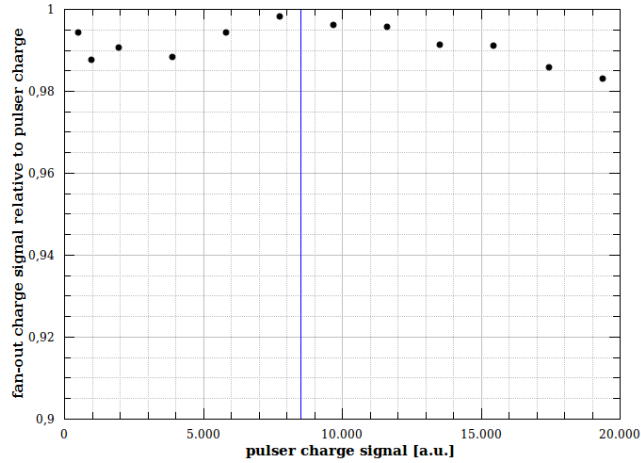
Figure 5.5: (Fan-out integral relative to the pulser integral. The plot range coincides with the oscilloscope range used; the blue line shows approximately the position of the highest pulses included in the analysis (these in the 140 keV-slice).

5.4.2 Oscilloscope linearity

Having the pulser data, I took the opportunity to check the linearity of the oscilloscope as well. The measurement procedure for this was the same as for the fan-out linearity test described above. But this time the analysis was concerned with the pulse heights instead of the pulse integrals. The heights recorded on the oscilloscope were fitted with a Gaussian function and the mean value was compared to the pulse amplitude adjusted on the pulse generator. The results are presented in fig. 5.6. For a single oscilloscope scale, the deviation from linearity was 0.2 %.

5.4.3 PMT linearity

The measurement of the PMT linearity was conducted in the MPIK's Faraday laboratory, an electromagnetically shielded darkroom. Among other uses it works as a test stand dedicated for large-scale tests of PMTs and electronics of the Double Chooz detectors.

For this measurement a laser diode emitting at 438 nm wavelength was utilized. It was operated at 1.0 % of its maximum power. From measurements by J. Haser the laser intensity is known to be sufficiently stable at low intensities [54]. The laser light is guided into the Faraday cage by means of an optical fiber, of which the end is pointed directly at the PMT (fig. 5.7). Changing the laser power to decrease the light intensity could introduce a new source of non-linearities.

Therefore I used a set of neutral filters of different transmissions to reduce
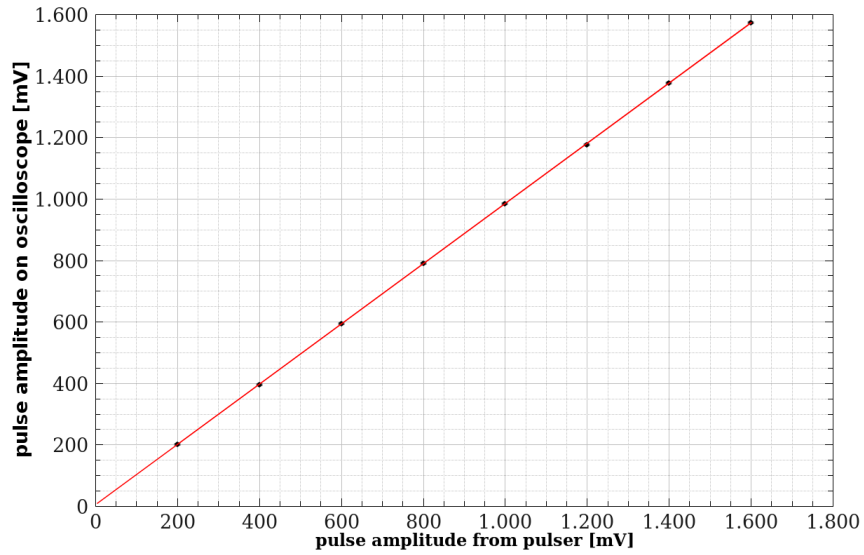
(a)
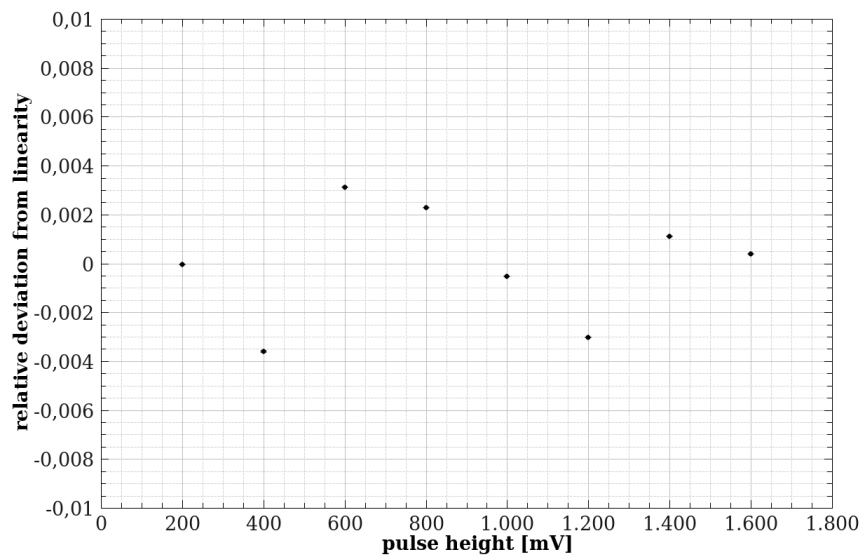
(b)

Figure 5.6: (a) Pulse amplitudes on the oscilloscope vs. pulse amplitudes set on the pulser. (b) Relative deviation of the oscilloscope pulse heights from linearity.
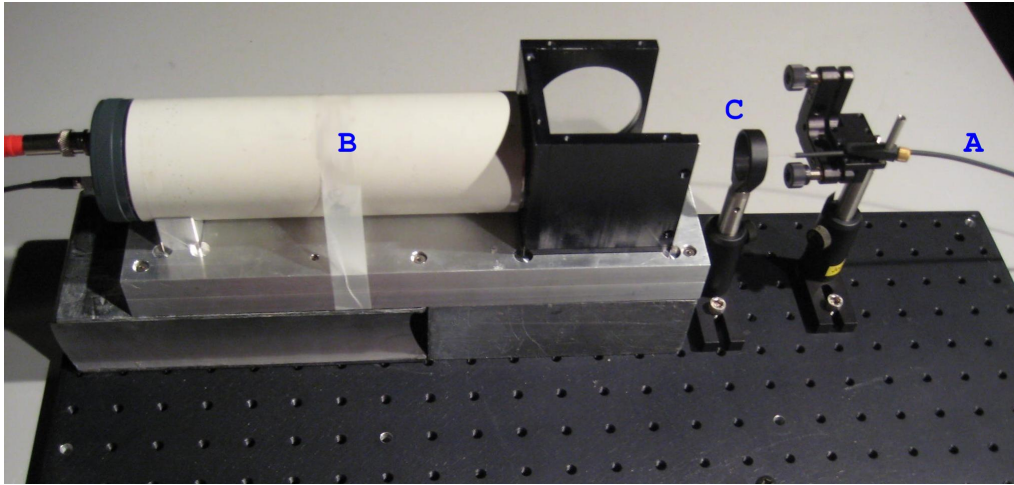
Figure 5.7: Setup for the linearity test of the PMT. On the right the optical fiber (A) can be seen, through which the laser light is guided in the direction of the PMT's sensitive area. The PMT (B) is mounted to the sample box for stability. On the stand (C) between fiber and PMT different filters can be mounted.

the intensity. The filter transmissions were measured wavelength-dependent with an UV-vis spectrometer by Ch. Aberle. The filters were mounted between the fiber end and the PMT. Great care has been taken to align the ray perpendicular to the filter plane and PMT surface respectively to minimize effects due to reflection. For the measurement, the filters were changed in succession. Then, for each filter used, 1000 events of the PMT output were recorded. After every two filters, a run without any filter was performed. As the PMT remained in the darkroom throughout the course of this experiment, the filter changes had to be done in complete darkness. Again, in the analysis the PMT voltage pulses were integrated to obtain the charge. The mean value of the narrow charge distribution was then determined by a Gauss fit to the distribution and plotted against the transmitted light intensity.

The test results are shown in fig. 5.8. The PMT output charge has proven to scale linearly with the light intensity. The deviations from linearity are 1.0 %. From the runs without any filters the fluctuations in the laser intensity could be controlled. Over the duration of the experiment, the standard deviation of the laser light intensity was 0.4 %. The PMT non-linearity in total was estimated to be 1.1 %.
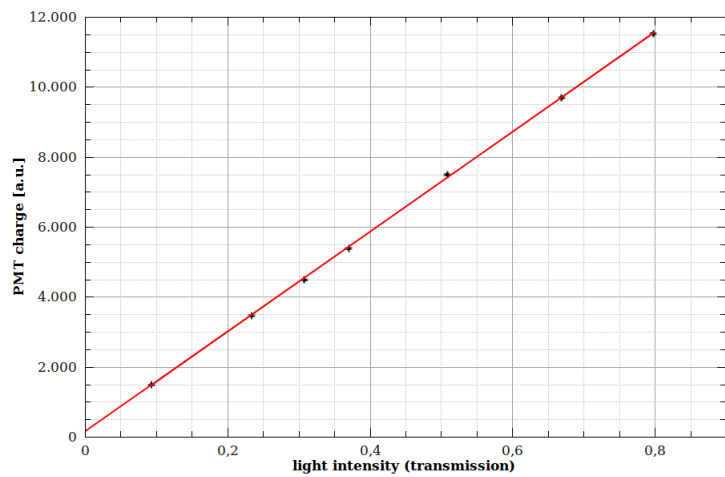
(a)
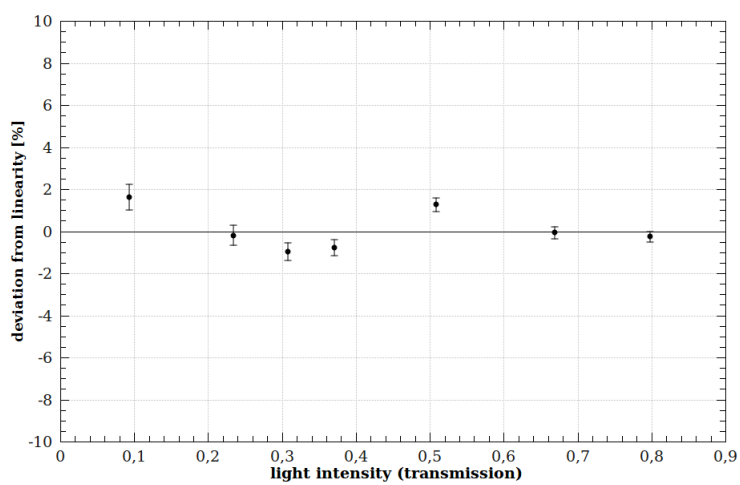
(b)

Figure 5.8: (a) PMT charge signal in dependance on the incident light intensity (b) relative deviation of the PMT charge from linearity.

5.5 Discriminator threshold

As the non-linear behavior of $L(E)$ is the more pronounced, the lower the electron energies are, one desires to take data points for electron energies as low as possible. These events are those events with such a small light yield that the PMT pulses just manage to pass the discriminator threshold. The threshold however can have an influence on the pulse distribution, so that the data points for the lowest electron energies are not reliable. Hence the question arose which energy slice can still be safely analyzed without acquisition of systematic errors due to the threshold effect.

For higher slices, where the peak is far from the threshold, the charge distribution follows approximately a Gaussian (see section 4.4.2 for details). In the case of low energy slices, the discriminator threshold should sharply cut the left part of the distribution, if one assumes identical PMT pulse forms and a stable baseline. In reality, variations of the baseline offset together with broader and narrower pulse forms populate the area around the threshold with events in a nontrivial distribution. The PMT baseline offset in this experiment showed a variation of 5 mV width. The resulting curve then differs from a pure Gaussian. A fit of such a curve with a normal distribution can drag the fitted mean value away from the "true" value. It is therefore important to know which slices are affected by the threshold effect.
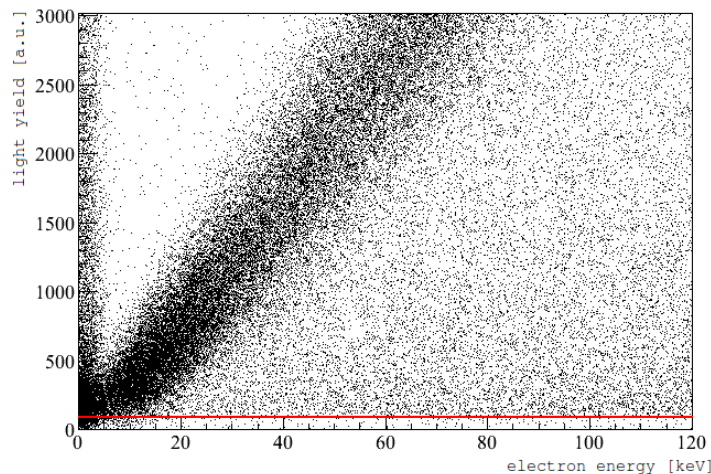
Figure 5.9: A close-up of the energy-light yield diagram (fig. 4.6). The region below the red line is only sporadically populated with events and identified as the discriminated region. Above energies of 18 keV the peak can be considered completely outside the discriminator region.
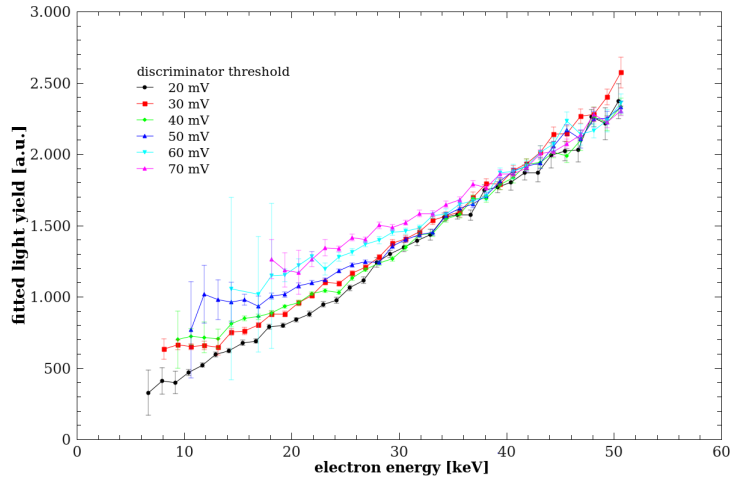
Figure 5.10: Light yield curves obtained from the energy slices for measurements with different discriminator thresholds.

An apparent and conservative suggestion would be that the fits for the mean value are unaffected by the threshold if the fit range excludes the discriminated region and the peak lies outside of this area. The discriminated region can be identified from the energy-light yield diagram (see fig. 5.9). To investigate if one could go down to even lower energies without biasing the results, I performed several complete measurements of the response function with different discriminator thresholds. In steps of 10 mV the threshold was lowered from 20 mV to 70 mV below the baseline position. For each measurement the complete analysis procedure had to be done. The configuration of section 4.3 was only altered in that just the 400 kBq ^{137}Cs source was used and placed directly under the cell. The measurement was conducted with the Double Chooz target scintillator. After the analysis procedure (section 4.4) the obtained mean values were plotted against the slice mean energy for each discriminator threshold set. The results are shown in fig. 5.10. When two curves merge, it can be concluded that the mean value obtained in this region is independent of the threshold, since a further decrease gives the same results. The points where two curves converge have then been obtained for curves of two following thresholds, and compared with the values that one would have extracted from fig. 5.9. These studies led to the conclusion that it is safer to only include those energy slices in the final analysis where the peak lies completely above the threshold. Therefore only energy slices from 19 keV upwards were considered in the final experiment.

53

5.6 Results of the studies of systematics

The overall influence of systematic effects was found to be low. The PMT was identified to be the biggest contributor to the total systematic error with a relative deviation from linearity of 1.0 %. The non-linearity of electronics, given by the non-linearity of the fan-out, was 0.4 %. The oscilloscope showed a total deviation from linearity of 0.2 %. These uncertainties sum up to 1.2 %. This is taken as the systematic error attributed to each datapoint in the final analysis, together with the statistical error.

Other sources of possible systematic effects could be neglected. The germanium spectrometer showed a relative deviation from linearity of less than 0.1 % which was not taken into account. The slice widths have been chosen to be 2 keV, which is slightly larger than the effective resolution of the germanium spectrometer. A systematic effect due to the slice width was not considered. The coupling, voltage adjustment and geometric configuration, which changed slightly during the preparation of each run, showed to have no visible effect on the measurement and could be neglected. The discriminator threshold produces a notable systematic effect, which however could be easily avoided by only including unaffected energy slices in the data analysis. The deterioration of the light yield with time is an undesired effect, but it is assumed to be of negligible influence for the determination of the quench parameter, as it seems to affect each slice equally and independent of the energy. Therefore it has also not been taken into account.

Chapter 6

Results

The response function $L(E)$ has to be characterized for each scintillator fluid used in the Double Chooz experiment. To do so, I checked if the experimental data can be described reasonably well by one of the models introduced in section 3.4 and extracted the respective quenching parameters that produce the best fit to the experimental data. Other measurements with α-particles have already been performed and the results for electrons and α-particles will be compared in section 6.3.

6.1 Samples

During the course of this thesis the different liquid scintillators used in the Double Chooz detector have been measured: the neutrino target, the gamma catcher and the muon veto. In addition to the Double Chooz scintillators I also measured $L(E)$ for the liquid scintillator of the Borexino experiment.

Target scintillator The target sample measured was the original mixture prepared for the Double Chooz detectors. It was produced at our institute and a certain quantity has been sidelined for measurement purposes including the ionization quenching studies. It is composed of 80 $\%_{vol}$ n-dodecane and 20 $\%_{vol}$ PXE, with the Gd-complex dissolved at a concentration of 1 g gadolinium per liter, and the fluors PPO and bis-MSB dissolved at 7 g/l and 20 mg/l respectively.

Gamma Catcher scintillators The gamma catcher is studied in two varieties, one with 2 g/l and one with 5 g/l PPO concentration. The latter is discussed as a backup option, but the 2 g/l PPO version is currently preferred. The smaller fluor concentration makes the mixture "slower", so that the scintillation pulse forms in the GC are different from scintillations in the target. This allows for pulse shape discrimination between target and GC events,

which can be useful for position reconstruction [24]. However, a concentration of 2 g/l is below the critical concentration c_{cr} (see section 3.2) and the light yield of the scintillator varies more with the concentration. 5 g/l would be beyond c_{cr} and the light yield would be practically insensitive to the concentration. This mixture is also less sensitive to quenching due to impurities.

The samples used in this work were prepared for long-term studies and material compatibility tests by U. Schwan and B. Gramlich. It had a composition of 66 %$_{\mathrm{vol}}$ Ondina 909, 30 % n-dodecane and 4 %$_{\mathrm{vol}}$ PXE. The bis-MSB concentration was 20.3 mg/l.

Veto scintillator The veto scintillator blend was produced at the Technische Universität München (TUM) and a sample was made available to us. In contrast to the mixture used in Double Chooz, the sample still did not contain any bis-MSB. The scintillator has been subjected to a purification procedure and there was the risk that the filter could also have held back some of the dissolved PPO. I therefore cross-checked the PPO concentration at our institute with the help of an absorption spectrometer.

For this purpose 20 μl of the veto sample were diluted in dodecane at a ratio of 1:500. The PPO molecules can then be regarded isolated and are to exhibit their characteristic absorption band between 320 nm and 450 nm. The other components do not absorb strongly in this wavelength region. The measurement was conducted with a Cary UV-Vis spectrometer. It exposes the sample to light of known intensity I_0 and wavelength and measures the intensity of the transmitted light $I(x)$. The sample is then scanned over a broad range of wavelenghts and the absorption spectrum $A(\lambda) = -\log_{10}(I/I_0)$ is recorded. $A(\lambda)$ is related to the concentration c through the molar extinction coefficient $\epsilon(\lambda)$:

$$\epsilon = \frac{AM}{cx},$$

with M being the molecular mass of the substance and x being the pathlength in the cell. The molar extinction coefficient $\epsilon(\lambda)$ of PPO is already known from spectroscopical studies on the Double Chooz chemicals done by myself in the context of an earlier research project. It could be confirmed that the PPO concentration in the sample still was the desired 3 g/l after filtering. In the end the desired amount of bis-MSB was weighed and added to the mixture so that the measured sample contained 20 g/l bis-MSB as used in Double Chooz.

Borexino scintillator The solar neutrino experiment Borexino uses a liquid scintillator consisting of PPO dissolved in pseudocumene (PC) at a concentration of 1.5 g/l. It is of special interest because of its simple composition

and because there is already data available. This scintillator could therefore be used as to cross-check the data from the Double Chooz scintillators.

The mixture has been reproduced in our chemistry laboratory with the original pseudocumene used in the Borexino experiment, taken from our stocks. Due to the age of the substance, the sample quality has been tested. The transparency was examined by means of absorption spectroscopy as described above and no deterioration could be found.

6.2 Curve fitting and determination of quench parameters

The experimental results now have to be checked for concordance with the models presented in 3.4. This is done with a fit of the curves predicted by the models in section 3.4 to the data points. The equations (3.4), (3.7) and (3.9) are functions of dE/dx, whereas the experimental data relates the light yield to the deposited energy E. I have written a C++ program that numerically integrates dE/dx and calculates ΔL for each step dx by the above equations and performs a χ^2-fit with kB and a scaling factor c_0 as fit parameters. Though the quenching parameters originally have different names in the different models, they are treated in this section solely as fit parameters and are referred to as "kB" independent of the model used.

The differential energy loss dE/dx is modelled as a continuous function by using the Berger-Seltzer formula (see section 3.3) and computed for small steps dx. In fact, three phases are differentiated to make sure that the energy loss per step remains low. For higher E_e the energy transferred to the medium is still low and a step size $dx_1 = 10$ nm is used. When E_e is lower than 1 keV, dE/dx increases and the step size is refined to the smaller value $dx_2 = 0.1$ nm. In comparison, the total range of a 100 keV electron is of the order of 100 μm. For electron energies below I the leading logarithmic term of (3.1) becomes negative, i.e. the electron would gain energy from the medium. Thus the formula is not valid for very small E_e. To eliminate this effect, the differential energy loss for $E_e \leq 100$ eV is modelled as a linear function interpolating (3.1) from zero to 100 eV as in [48]. The density effect and bremsstrahlung losses are neglected.

The mean ionization energy I is documented for elements and some compounds in frequent use [55]; for other substances it can be calculated from these data via

$$\ln I_{\text{sample}} = \frac{\sum w_i \frac{Z_i}{A_i} \ln I_i}{\sum w_i \frac{Z_i}{A_i}} \tag{6.1}$$
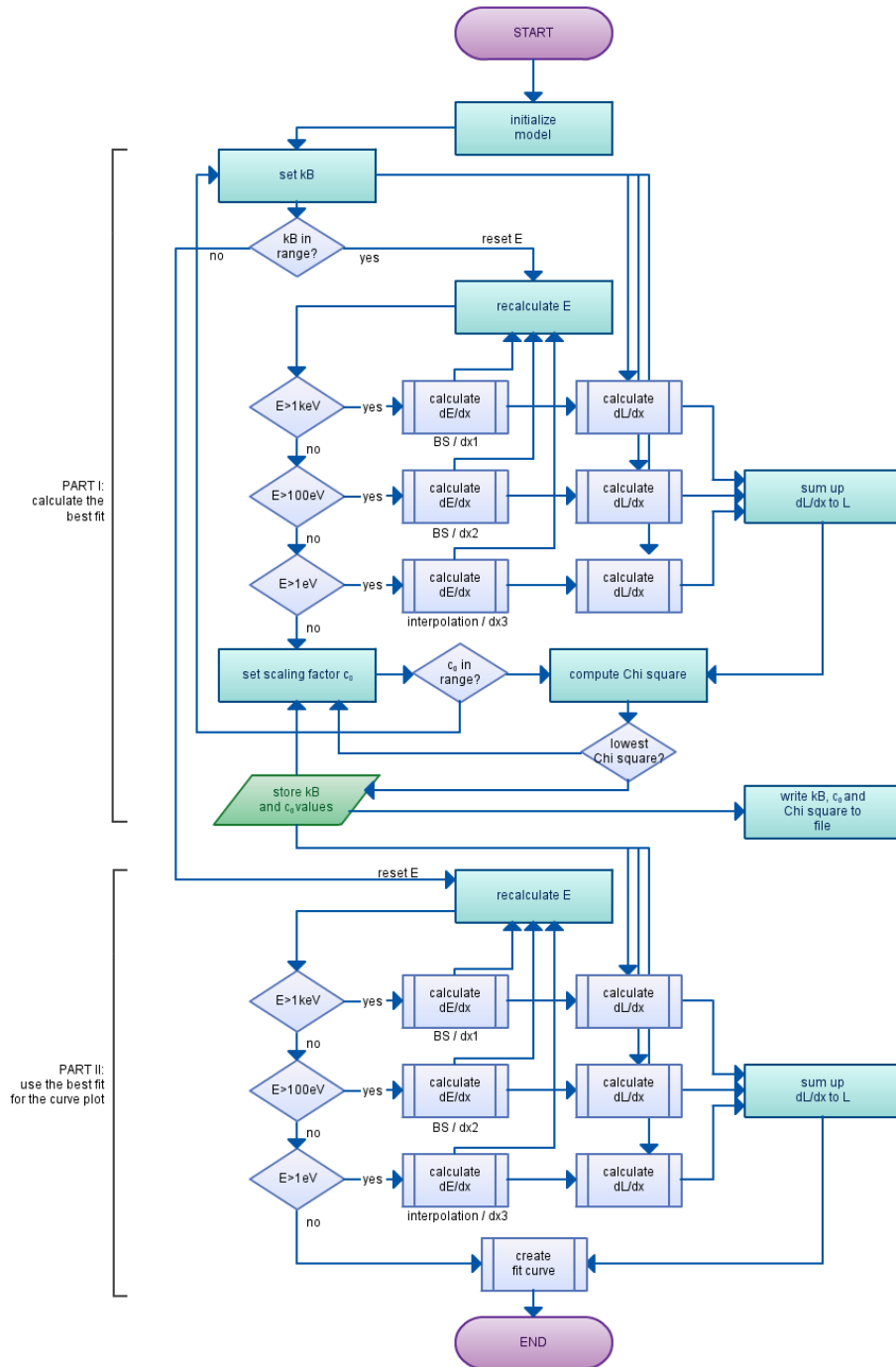
Figure 6.1: Structure of the fitting program.

where w_i is the fraction by weight of the respective elements in the mixture [39]. n_e can also be calculated from the composition.

A flowchart of the program structure can be seen in fig. 6.1. First, the electron energy is set to the highest value for which data was taken, i.e. the energy value of the highest slice included in our analysis. For a given kB the program then computes dE/dx as described above and determines the differential light yield dL/dx as predicted by the quenching model. Which of the models is used is selected at the initialization stage. The electron energy is then sequentially reduced by the value calculated and the ΔL are summed up to obtain the total light yield L_{kB}. The process is repeated until E_e drops below 1 eV, then kB is varied and the procedure is iterated with the new value. The fit quality is determined by a minimization of

$$\chi^2_{kB} = \sum_{i=1}^{n} \frac{[L(E_i) - c_0 L_{kB}(E_i)]^2}{\sigma^2_{L(E_i)}}. \tag{6.2}$$

$L(E_i)$ is the measured light yield for electrons of energy E_i, and the $\sigma_{L(E_i)}$ are the associated uncertainties, composed of the statistical and the systematic error (see chapter 5). $L_{kB}(E_i)$ is the computed light yield for a given kB and electron starting energy E_i. c_0 is a scaling factor. It is treated as a second fit parameter and for each value of kB the factor c_0 is varied until (6.2) is minimal. The kB and c_0 values corresponding to the global χ^2-minimum are the fit results. With these values fixed, the process is repeated once more to get a graphical fit curve.

In the analysis of the light yield function the lowest energy slice considered is the 19 keV slice (see section 5.5 for details). The highest slice included is the one of 139 keV energy, due to the little statistics available in the region farther above. This limitation also makes sure to exclude Čerenkov radiation, which would be an issue at energies above 160 keV. The results for the different scintillators are presented in the following section.

6.3   Results

The values obtained from the scintillator measurements are compiled in table 6.1 and the graphical representations can be seen on the plots on figures 6.2 to 6.6. In the standard plots of the light yield against the electron energy the curvature is hardly visible. For a better visualization of the non-linearity of the response function, a representation has been chosen that relates the actual light yield to the light yield expected in the case of a totally linear behavior (i.e. $kB = 0$ and thus $dL/dx \sim dE/dx$). Assuming that the data points above 100 keV are already in the linear region, the data points from there to 139 keV have been fitted with

a linear function. The so determined light yield of the 139 keV data point has been considered a reference point, which has been connected with the origin by a line. The light yields of the data points have been set in relation to this line and the ratios are plotted against the corresponding electron energy in a new plot (figs. 6.2b to 6.6b). The pronounced deviation from linearity for electrons below 100 keV kinetic energy can now clearly be seen. These plots are for visualization purposes only and no calculations or fits have been done based on them.

SCINTILLATOR	MODEL		
	Birks [cm/MeV]	Voltz [cm/MeV]	Wright [cm/MeV]
Target	$0.0159^{+0.0042}_{-0.0037}$	$0.0122^{+0.0026}_{-0.0025}$	$0.0372^{+0.0112}_{-0.0090}$
red. Chi square	0.99	0.83	1.09
GC (2 g/l PPO)	$0.0292^{+0.0058}_{-0.0053}$	$0.0198^{+0.0031}_{-0.0028}$	$0.074^{+0.018}_{-0.015}$
red. Chi square	1.47	2.16	1.72
GC (5 g/l PPO)	$0.0244^{+0.0058}_{-0.0050}$	$0.0176^{+0.0031}_{-0.0031}$	$0.0602^{+0.0166}_{-0.0141}$
red. Chi square	1.28	1.14	1.39
Veto	$0.0153^{+0.0042}_{-0.0037}$	$0.0118^{+0.0026}_{-0.0025}$	$0.0357^{+0.0112}_{-0.0029}$
red. Chi square	1.13	1.05	1.20
Borexino	$0.0171^{+0.0041}_{-0.0036}$	$0.0127^{+0.0024}_{-0.0023}$	$0.0411^{+0.0011}_{-0.0039}$
red. Chi square	1.03	1.31	0.90

Table 6.1: Results for the quenching parameters of the different models, as obtained with the Berger-Seltzer formula. As the equations are of distinct mathematical forms, the quenching parameters cannot be directly compared between the models. The χ^2 values correspond to 59 degrees of freedom.

In general, all models describe the scintillation behavior in the investigated energy range reasonably well. All three models yield very similar curves. This may seem surprising at the first sight, as they have totally different formal representations ((3.4),(3.7) and (3.9)). A closer look shows that these formulae have the same first-order expansion [27].

Of the liquid scintillators, the GC with 2 g/l PPO is the most affected by ionization quenching. As the concentration of the primary fluor is low, the solvent-solute energy transfer has to compete more with the ionization quenching mechanism. From a comparison with the 5 g/l-version one can see experimentally that a higher fluor concentration diminishes the ionization quenching, as it is expected. The Borexino scintillator with only 1.5 g/l PPO has an even lower fluor concen-
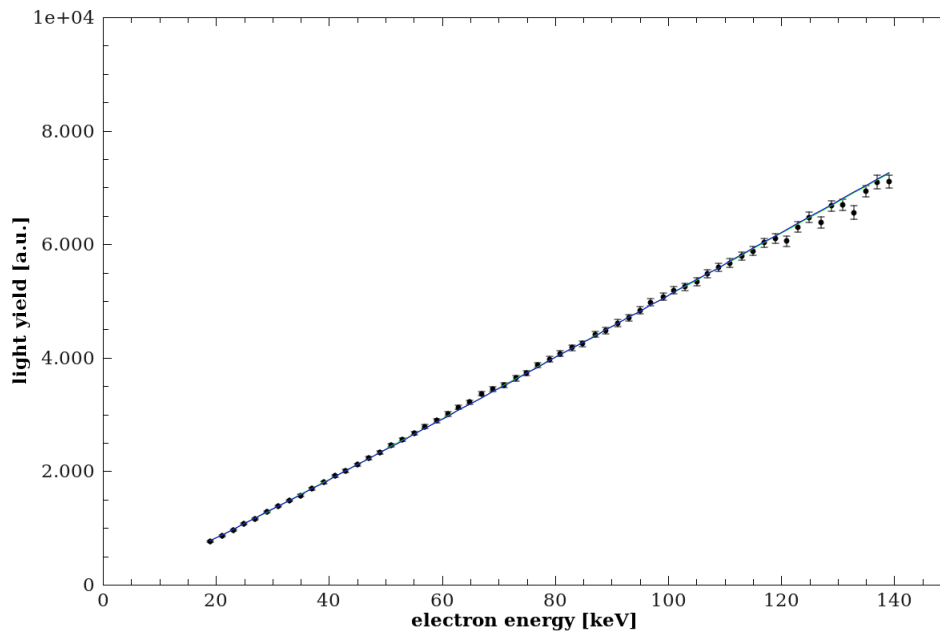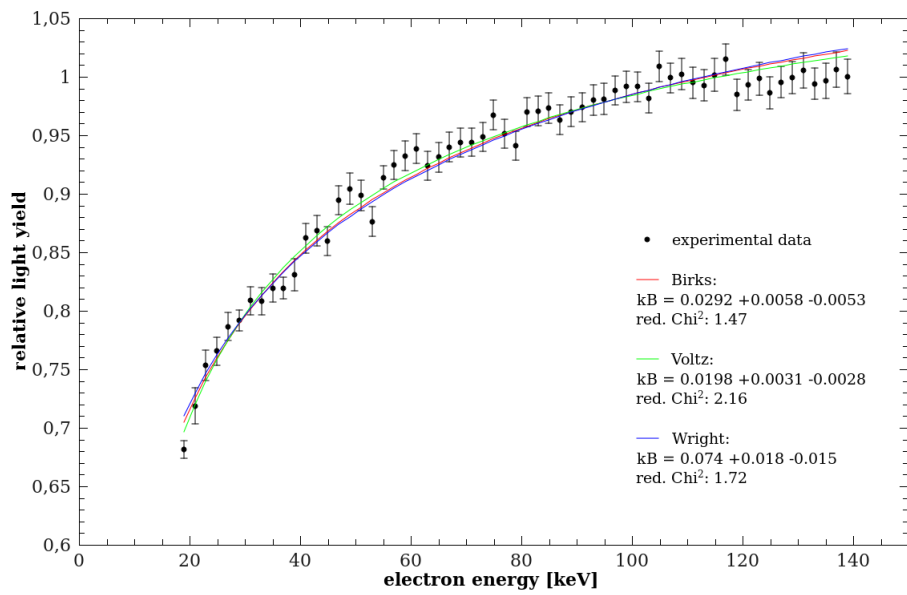
(a) linear plot
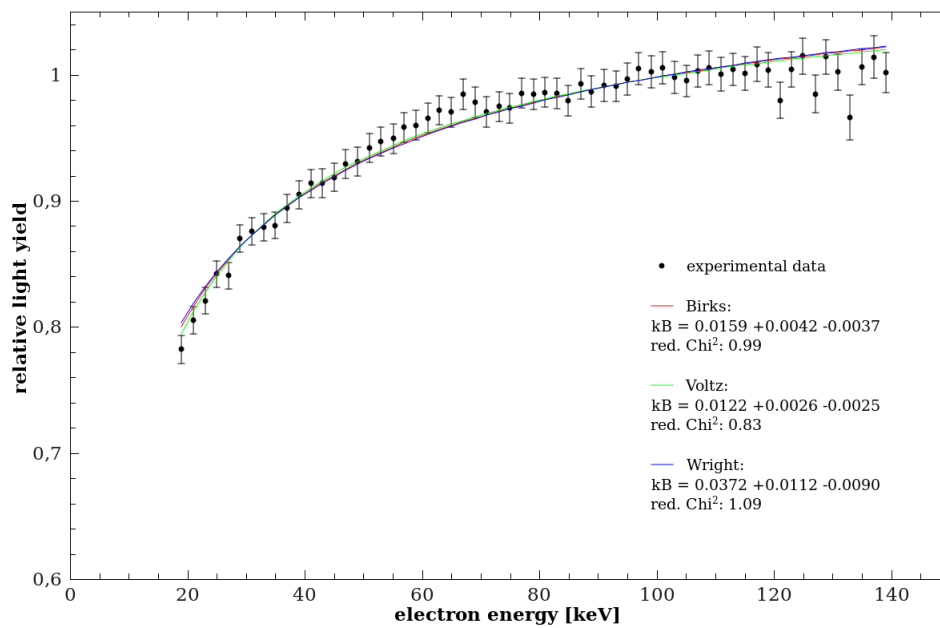
(b) relative plot
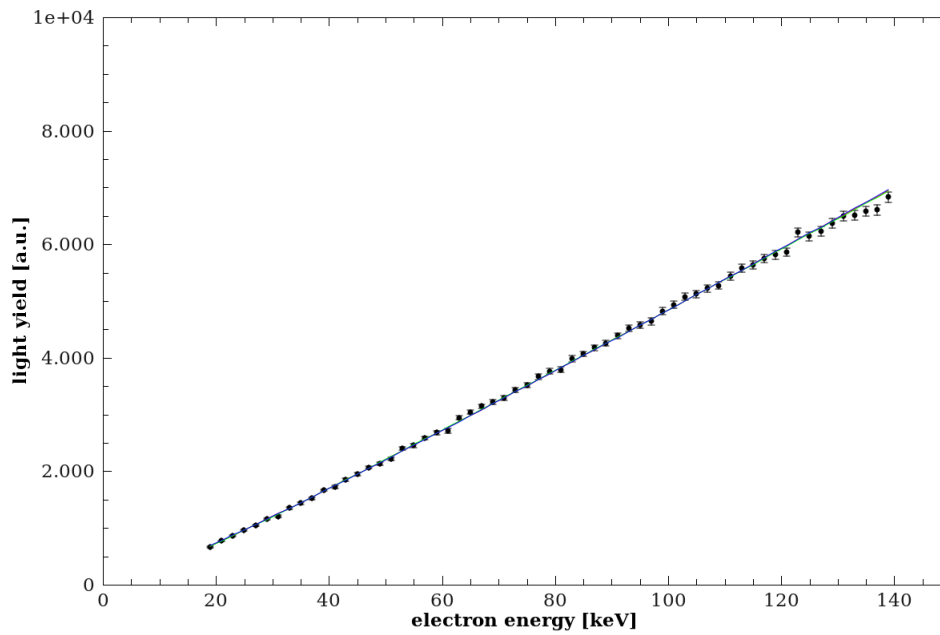
Figure 6.2: Results for the Target scintillator.
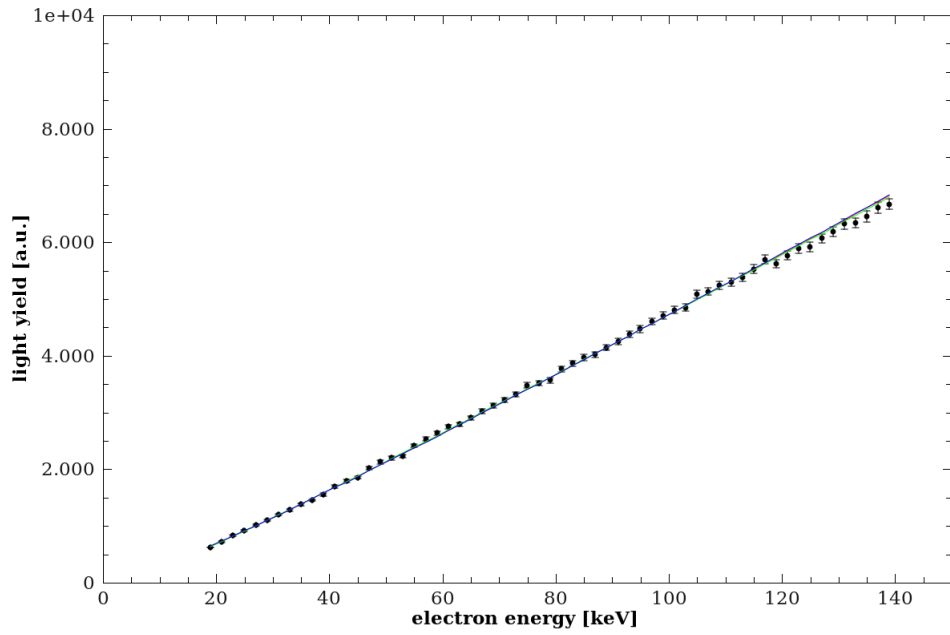
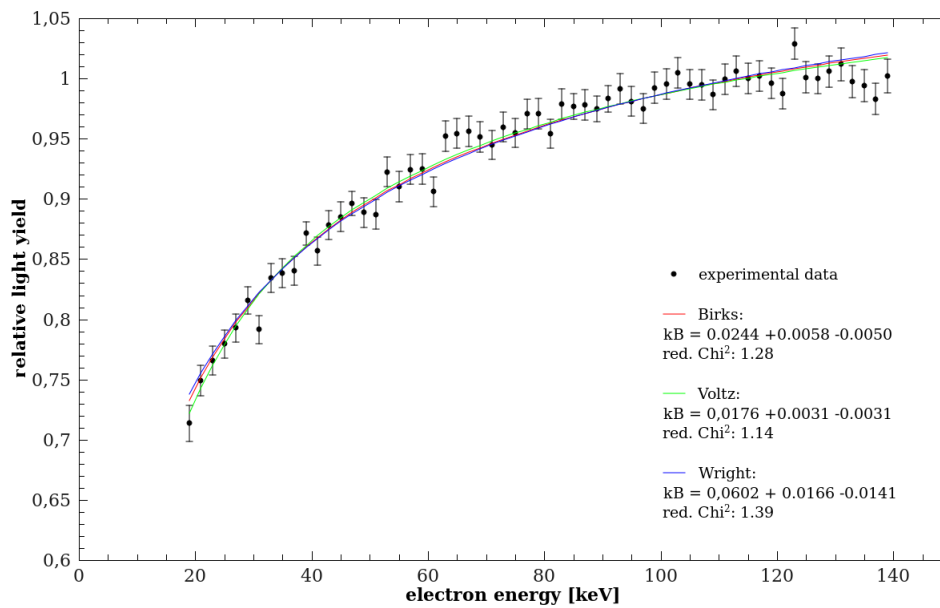**(a)** linear plot

(b) relative plot

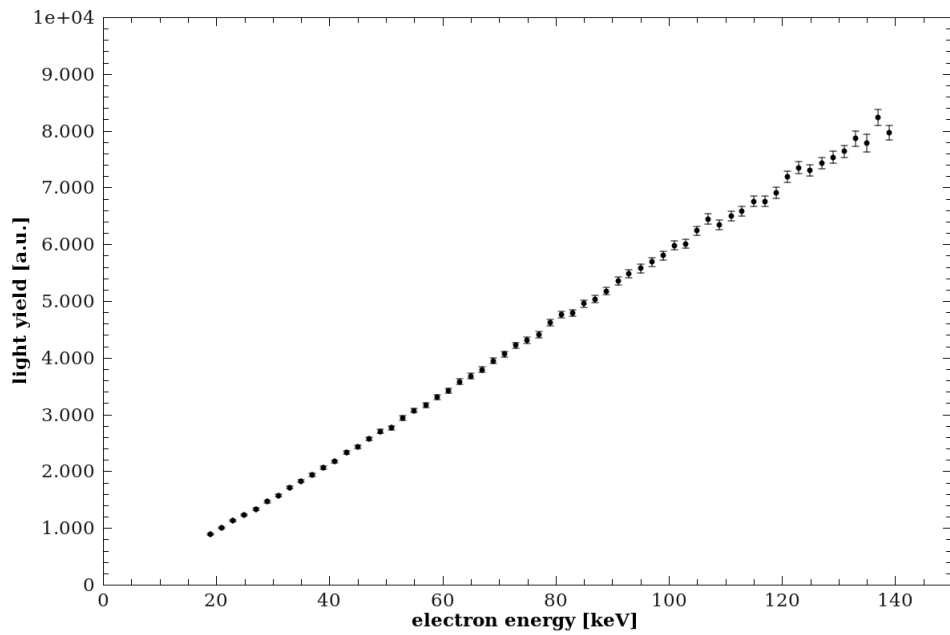**Figure 6.3:** Results for the Gamma Catcher scintillator (2 g/l PPO).

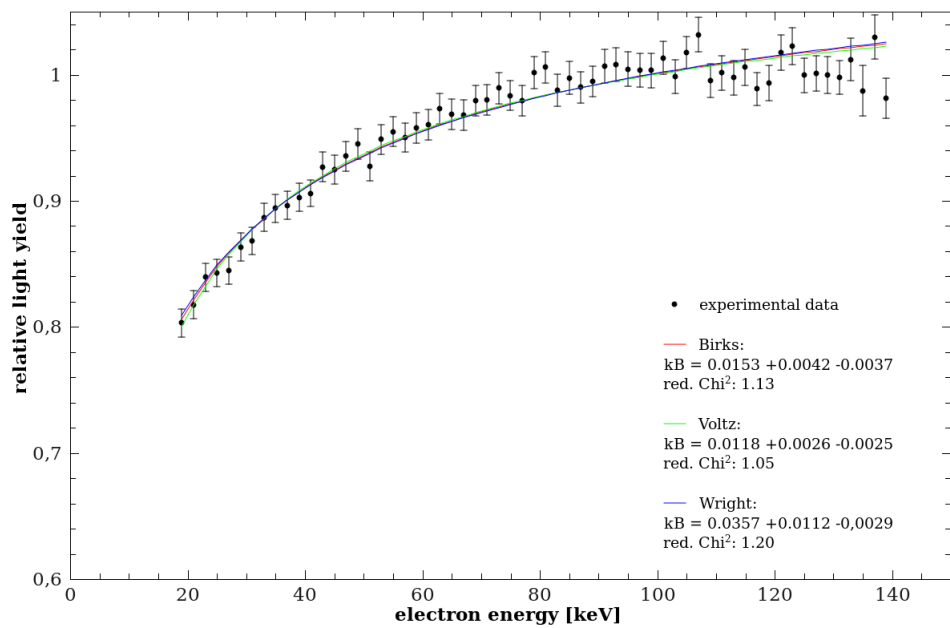**(a)** linear plot

(b) relative plot

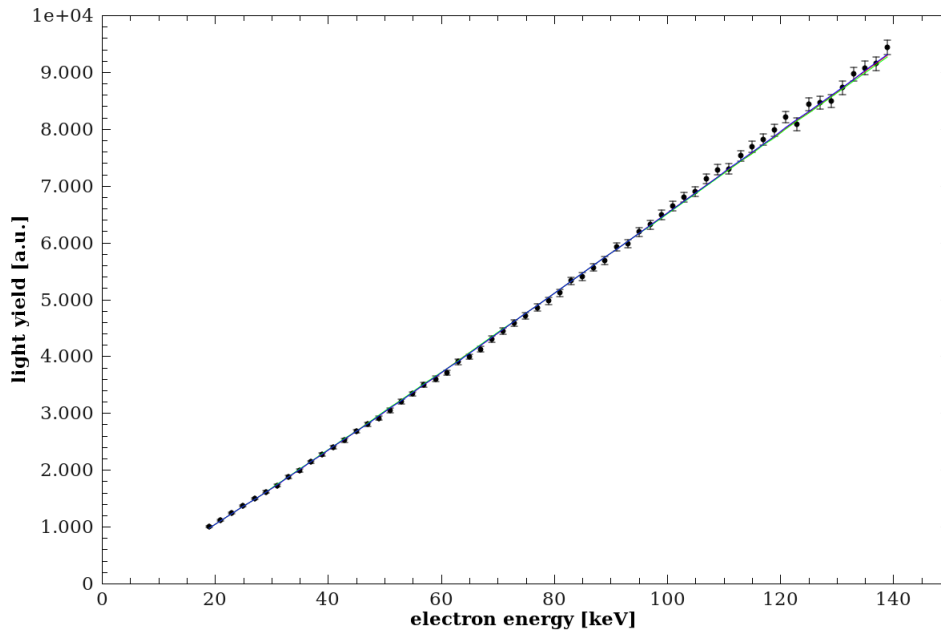**Figure 6.4:** Results for the Gamma Catcher scintillator (5 g/l PPO).

(a) linear plot

(b) relative plot

**Figure 6.5:** Results for the Veto scintillator.

(a) linear plot
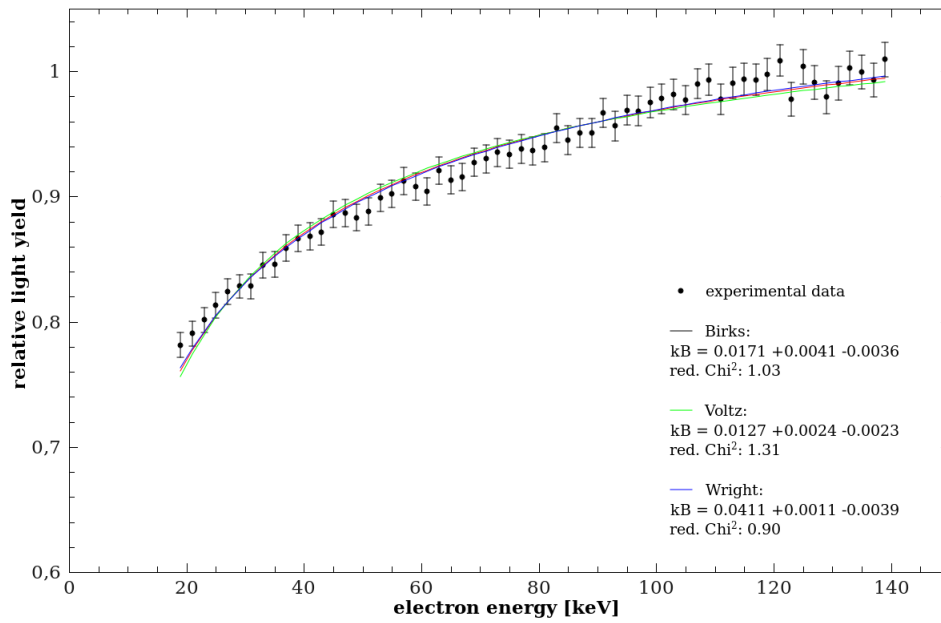
(b) relative plot

Figure 6.6: Results for the Borexino scintillator.

65

tration, but a small quenching parameter due to the different solvent. The energy transfer between PC and PPO is very effective and the critical concentration is lower in this mixture. Therefore the ionization quenching cannot compete much with the energy transfer, even at a smaller fluor concentration.

In the case of the target it is the non-scintillating Gd-complex that is responsible for the low quench parameter. The presence of the organic Gd-molecules opens another energy transfer path. This reduces the overall light yield of the mixture, as the energy transfer to the PPO already has to compete with the transfer to the Gd-complex. But it also reduces the influence of the ionization quenching, as the energy transfer to the Gd-complex takes longer than the transfer to PPO. Because of this, the competition particularly affects the slow part, while the fast part can reach the PPO practically unquenched and lead to scintillation. The ionization quenching now acts on a similar time scale as the transfer to the Gd-complex, when the fast part of the time spectrum has already lead to scintillation. For the veto no predictions could be made in advance, as no results from timing measurements were available for this mixture. From the small value of the quenching parameter it looks like the energy transfer path from LAB to PPO is very effective.

Next point to mention is that the minimal χ^2 do not indicate a preference for a specific model; the results are comparable. The values of the reduced χ^2 show that the experimental data is fit well and that the predictions of the different models are in good concordance with the data. However, it was observed that the fit curves have a systematic deviation from the experimental data. On residual plots in figs. 6.7a to 6.9a, the relative distances of the data points from the Birks curve are shown. Interestingly, the Borexino scintillator is an exception, in that the residuals show a distribution with a bent-down curvature, while the residuals of the Double Chooz scintillators show a distribution which is curved upwards. This difference between the Borexino scintillator and the other scintillators is not fully understood at this moment and requires further investigation.

Ch. Aberle conducted kB measurements with α-particles. The scintillation response was measured for the four α-energies 5.3 MeV, 5.5 MeV, 6.0 MeV and 7.7 MeV with α-sources directly dissolved in the liquid. In this measurement the light yield spectrum was recorded and the appearing peaks were attributed to the specific α-energies. The analysis of the data with help of the Birks model yielded quenching parameters of 0.0101 ± 0.0010 cm/MeV for the target, 0.0141 ± 0.0012 cm/MeV for the GC (2 g/l PPO), 0.0123 ± 0.0015 cm/MeV for GC (5 g/l PPO) and 0.0107 ± 0.0010 cm/MeV for the veto. Again, the GC (2 g/l PPO) mixture shows the highest quenching factor, followed by the GC with 5 g/l PPO. Target and veto show the least influence of the ionization quench effect. These values are systematically lower than the ones obtained with the Compton electron experiment. This behavior is not expected in the framework of the Birks model, since it only considers a dependance on dE/dx. Nevertheless, the effect
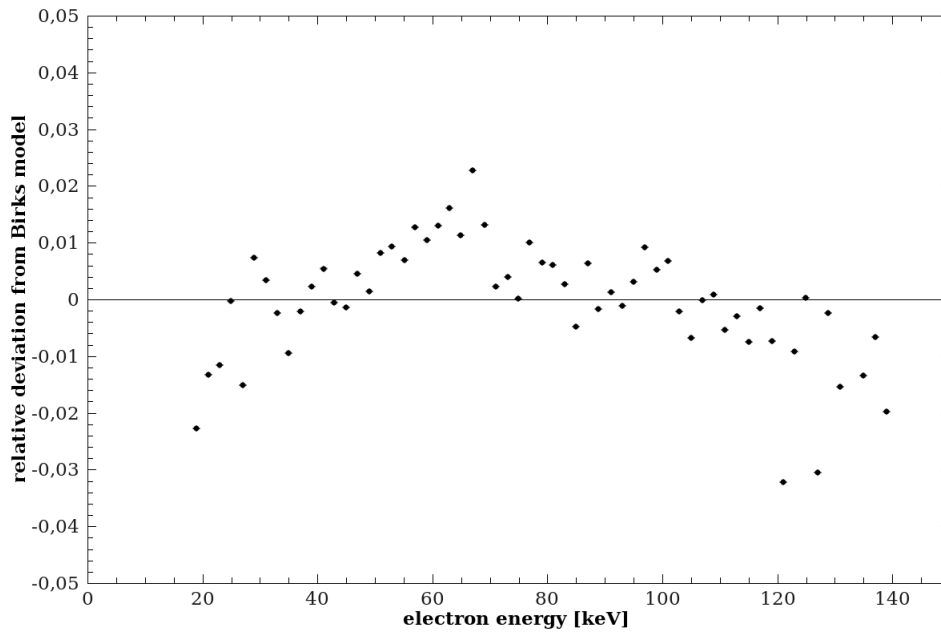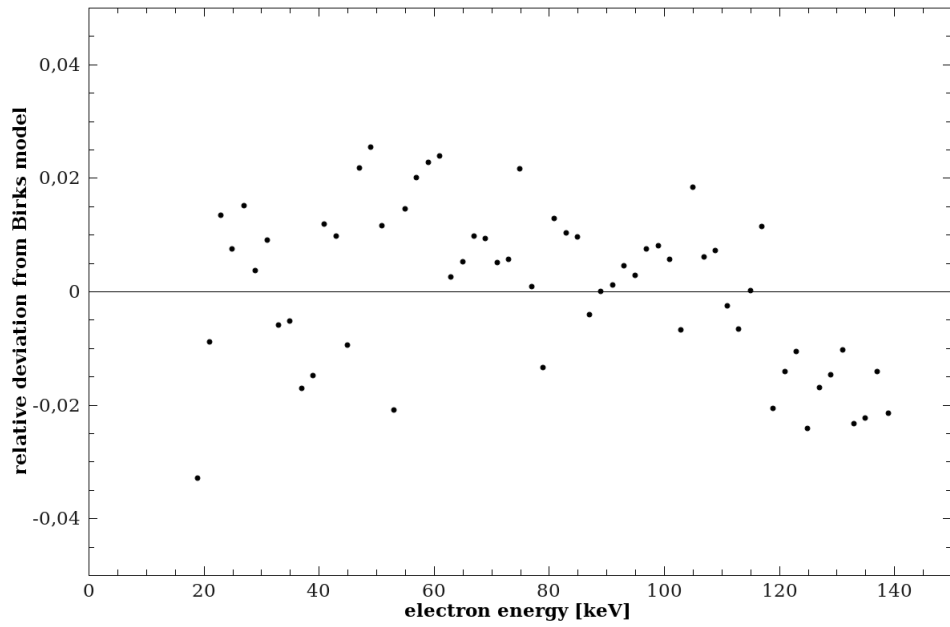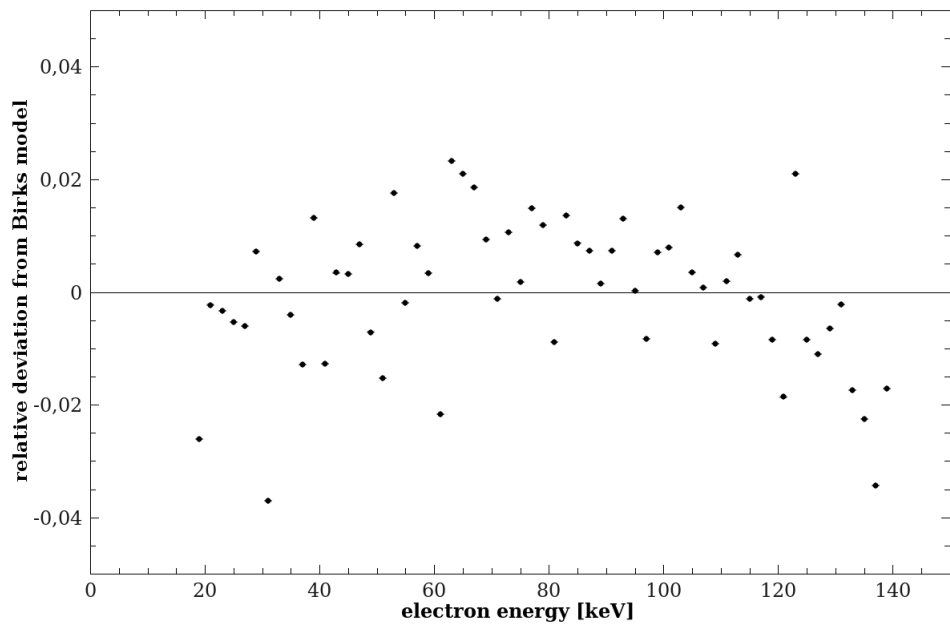
(a) Target
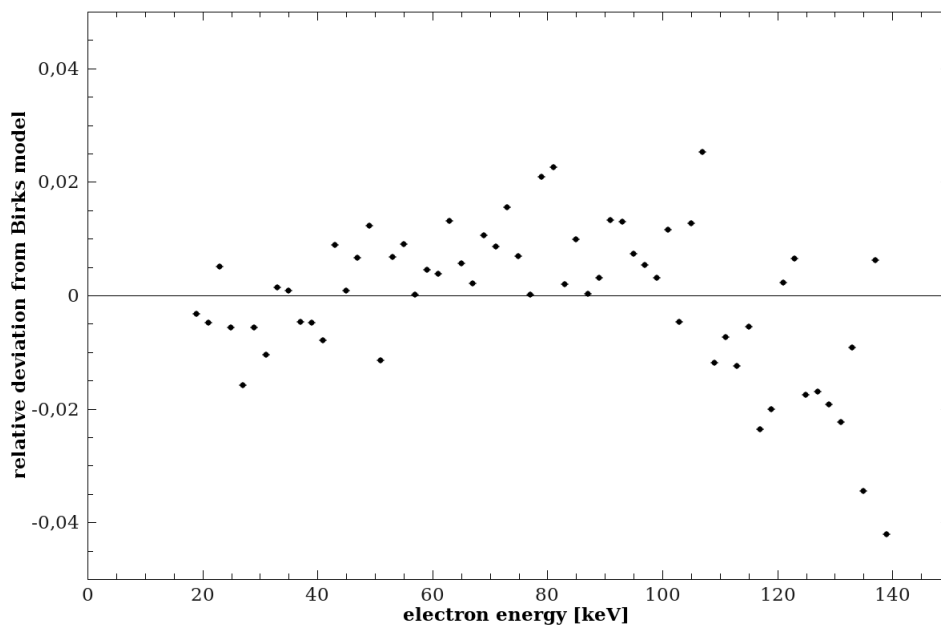
(b) Veto

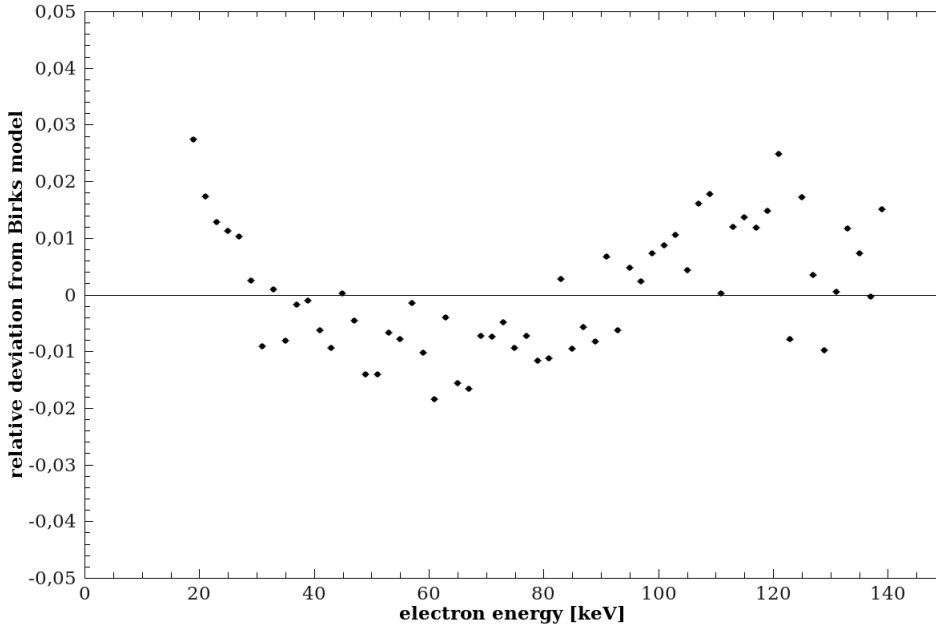**Figure 6.7:** Residual plots of the fit curves

(a) GC 2 g/l

(b) GC 5 g/l

Figure 6.8: Residual plots of the fit curves

Figure 6.9: Residual plots of the fit curves

can be explained qualitatively: Recent simulations in Geant4, also performed by Ch. Aberle, have show that α-particles do not produce secondary electrons with an energy high enough that they could leave the ionization column. Electrons, on the other hand, still have a certain probability to create δ-electrons which receive considerable energies. These secondary electrons can leave the ionization column, which contradicts the assumption made for incident electrons in 3.9. When a δ-electron was created, there are two electrons in the scintillator, which are each affected by ionization quenching when dE/dx gets high at the end of the particle track. Therefore the total quenching effect is stronger for electrons.

For the Veto scintillator a detailed simulation with δ-electron production was used to calculate the energy loss of electrons. A fit with the Birks law and the results of this simulation to the experimental data gave $kB = 0.0114 \pm 0.0015$ [56], which is compatible with the value obtained from the α-measurements. The production of secondary electrons also takes place in the measurement. It is however not included in the fit program described in 6.2. It neglects the additional quenching by δ-electrons and therefore underestimates the total quenching effect. To compensate for this, the fit converges to a higher value of kB, which is in better concordance with the data. Further investigations and simulations with explicit δ-electron creation are in progress.

6.4 Conclusions

It can be remarked that a particular value of kB always depends on the specific energy deposition mechanism and analysis mechanism employed. The experimental data obtained in this work can be analyzed with different models and simulations, which yield different results for the parameters. In this analysis, the kB values in table 6.1 refer to the Berger-Seltzer energy loss formula (3.1) without the creation of δ-electrons. The comparison of values for kB is only possible if they are obtained via the same analysis procedure.

The current model used in the Double Chooz Monte Carlo simulation is the Birks-model. The kB values currently implemented in the DC software come from α-measurements. The use of two different kB values for electrons and α-particles has to be considered.

Based on the results of the measurements performed in the framework of this thesis, it can also be said that apparently neither model has an advantage over another, considering the quality of the prediction. An advantage of the Birks model would be its simplicity. If the Birks model is pursued further, the quenching parameters have to be adjusted for each particle type. Further studies could help to understand the difference between the kB values for α-particles and electrons in more detail. With a better simulation of electron ionization quenching this work will contribute to the improvement of the energy reconstruction in the Double Chooz project.

Chapter 7

Summary

Neutrino oscillations are an important phenomenon to investigate physics beyond the Standard Model. The neutrino mixing is controlled by the PMNS matrix, of which two of the three mixing angles are known from experiments with solar, atmospheric, reactor and accelerator neutrinos. There is only an upper limit on the third neutrino mixing angle θ_{13} and several experiments are currently constructed to measure θ_{13}.

The reactor neutrino experiment Double Chooz aims to measure θ_{13} with a sensitivity of $\sin^2 2\theta_{13} = 0.03$. It employs two large-volume liquid scintillation detectors to measure the electron antineutrino flux from two nuclear reactors by the inverse β-decay in a novel Gd-loaded scintillator. The neutrinos are detected via the scintillation light created by the reaction products. For the analysis of the Double Chooz data, the light output of the scintillator has to be known in dependence of the particle energy. This relation is known to be non-linear for low particle energies because of the ionization quenching effect, the decrease in light yield due to mutual interactions of excited molecules.

To characterize the response of the liquid scintillators to low energy electrons, an experiment has been set up, in which electrons are created in the scintillator by Compton-scattering of γ-rays. The electrons produce scintillation light, which is observed by a PMT, while the energy of the scattered photon is measured in a germanium spectrometer. With this setup the light output of electrons with energies between 19 keV and 139 keV could be measured. A program has been written to analyze the events recorded in the measurement and several algorithms were implemented to remove defective events. Possible systematic effects have been thoroughly investigated. In linearity tests, the photomultiplier was identified as the principal source of systematic errors. Corresponding studies showed that the fan-out and the oscilloscope also contribute to the systematics. Some effects have been proven to be negligible. The overall systematic error on the data was 1.1 %.

The light yield curves have been measured for the Double Chooz liquid scintillators and the Borexino scintillator. Several models exist to describe the quench-

ing effect in terms of a single parameter. These models were tested for concordance with the experimental data via a self-written fit program. From the fits to the data the respective quench parameters could be obtained. The models were in good agreement with the experimental data and are suited for a use in the Double Chooz project. The results for the quenching parameters of the individual scintillators could be explained by energy transfer considerations. This work will help to improve the insights into the ionization quenching effect and the quality of the energy reconstruction in Double Chooz.

List of Figures

74

List of Tables

Bibliography

[1] F. Reines and C. L. Cowan, "The neutrino," *Nature*, vol. 178, pp. 446–449, 1956.

[2] R. Davis, D. S. Harmer, and K. C. Hoffman, "Search for Neutrinos from the Sun," *Phys. Rev. Lett.*, vol. 20, no. 21, pp. 1205–1209, 1968.

[3] B. Pontecorvo Жур. Экс. Теор. Физ. , vol. 33, p. 549, 1957. [*Sov. Phys. - J. Exp. Theor. Phys.*, vol. 6, pp. 429ff, 1958].

[4] R. N. Mohapatra and P. B. Pal, *Massive Neutrinos In Physics And Astrophysics*, vol. 60 of *World Scientific Lecture Notes in Physics*. World Scientific, 1998.

[5] B. Aharmim et al., "Independent Measurement of the Total Active ^{8}B Solar Neutrino Flux Using an Array of ^{3}He Proportional Counters at the Sudbury Neutrino Observatory," *Phys. Rev. Letters*, vol. 101, no. 11, p. 111301, 2008.

[6] C. Amsler et al., "Particle listings," *Phys. Let. B*, vol. 667, p. 1, 2008 (partial update 2009).

[7] Y. Ashie et al., "Measurement of atmospheric neutrino oscillation parameters by Super-Kamiokande I," *Phys. Rev. D*, vol. 71, no. 11, p. 112005, 2005.

[8] M. C. Gonzalez-Garcia and M. Maltoni, "Phenomenology with massive neutrinos," *Phys. Rep.*, vol. 460, no. 1–3, pp. 1–129, 2008.

[9] M. Apollonio et al., "Search for neutrino oscillations on a long base-line at the Chooz nuclear power station," *Eur. Phys. J. C*, vol. 27, no. 3, pp. 331–374, 2003.

[10] G. L. Fogli, E. Lisi, A. Marrone, A. Palazzo, and A. M. Rotunno, "Neutrino oscillations, global analysis and θ_{13}," 2009. arXiv.org:0905.3549.

[11] B. Aharmim et al., "Low energy threshold analysis of the phase I and phase II data sets of the Sudbury Neutrino Observatory," 2009. arXiv.org:0910.2984v1.

[12] W. Buchmüller, R. D. Peccei, and T. Yanagida, "Leptogenesis as the origin of matter," *Ann. Rev. Nucl. Part. Sci.*, no. 55, pp. 311–355, 2005.

[13] C. H. Albright and M. C. Chen, "Model predictions for neutrino oscillation parameters," *Phys. Rev. D*, vol. 74, no. 11, p. 113006, 2006.

[14] Ch. Kraus et al., "Final results from phase II of the Mainz neutrino mass searchin tritium β-decay," *Eur. Phys. J. C*, vol. 40, no. 4, pp. 447–468, 2005.

[15] T. J. Loredo and D. Q. Lamb, "Bayesian analysis of neutrinos observed from supernova SN 1987A," *Phys. Rev. D*, vol. 65, no. 6, p. 063002, 2002.

[16] KATRIN collaboration *Int. J. Mass Spectrom.*, vol. 251, no. 2–3, 2006.

[17] F. Gatti et al., 2006. crio.mib.infn.it/wig/silicini/proposal/.

[18] F. X. Hartmann and R. A. Naumann, "High temperature gas proportional detector techniques and application to the neutrino mass limit using ^{163}Ho," *Nucl. Instr. Meth. Phys. Res. A*, vol. 313, pp. 237–259, 1992.

[19] F. X. Hartmann and R. A. Naumann, "Observation of N and M orbital-electron capture in the decay of ^{163}Ho," *Phys. Rev. C*, vol. 31, no. 4, pp. 1594–1596, 1985.

[20] F. Ardellier et al., "Double Chooz: A search for the neutrino mixing angle θ_{13}," 2006. arxiv.org:0606025.

[21] C. Buck, F. X. Hartmann, D. Motta, S. Schönert, and U. Schwan, "Metal beta-diketone scintillators," in *Presentation at the Workshop on Future Low Energy Neutrino Experiments, TU Munich, Munich*, 2003.

[22] F. X. Hartmann, "Low Level Scintillators and Gadolinium," in *Presentation at the Workshop on Future Low Energy Neutrino Experiments, TU Munich, Munich*, 2003.

[23] C. Buck, *Development of metal loaded scintillators for future detectors to investigate neutrino properties.* PhD thesis, Ruprecht-Karls-Universität Heidelberg, 2004.

[24] C. Aberle, "Optimierung der Fluoreszenzcharakteristik von Flüssigszintillatoren des Double Chooz Reaktorneutrinoexperiments," Diploma thesis, Ruprecht-Karls-Universität, 2008.

[25] C. Buck, F. X. Hartmann, D. Motta, and S. Schönert, "Energy transfer and light yield properties of a new highly loaded indium(III) β-diketone organic scintillator system," *Chem. Phys. Letters*, vol. 435, no. 4–6, pp. 255–256, 2007.

[26] D. Motta, C. Buck, F. X. Hartmann, T. Lasserre, S. Schönert, and U. Schwan, "Prototype scintillator cell for an In-based solar neutrino detector," *Nucl. Instr. Meth. Phys. Res. A*, vol. 547, no. 2–3, pp. 368–388, 2005.

[27] F. D. Brooks, "Development of organic scintillators," *Nucl. Instr. Meth.*, vol. 162, no. 1–3, pp. 477–505, 1979.

[28] J. B. Birks, *The Theory and Practice of Scintillation Counting.* Pergamon Press, 1964.

[29] J. B. Birks, *Photophysics of aromatic molecules.* Wiley & Sons, 1970.

[30] R. Voltz and G. Laustriat, "Radioluminescence des milieux organiques I. Étude cinétique," *J. Phys. France*, vol. 29, no. 2–3, pp. 159–166, 1968.

[31] C. T. Peng and D. L. Horrocks, ed., *Liquid scintillator solvents*, Academic Press, 1970.

[32] F. H. Brown, M. Furst, and H. Kallmann, "Light and high energy induced energy transfer in liquid and rigid organic scintillators," *Discuss. Faraday Soc.*, no. 27, pp. 43–56, 1959.

[33] C. T. Peng, *Sample Preparation in Liquid Scintillation Counting.* The Radiochemical Centre Ltd., 1977.

[34] D. L. Horrocks, *Applications of Liquid Scintillation Counting.* Academic Press, 1974.

[35] T. Förster, "Zwischenmolekulare Energiewanderung und Fluoreszenz," *Annalen d. Physik*, vol. 437, no. 1–2, pp. 55–75, 1948.

[36] T. Förster, "Transfer mechanisms of electronic excitation," *Discuss. Faraday Soc.*, no. 27, pp. 7–17, 1959.

[37] D. L. Dexter, "A theory of sensitized luminescence in solids," *J. Chem. Phys.*, vol. 21, no. 5, pp. 836–850, 1953.

[38] D. L. Andrews, "A unified theory of radiative and radiationless molecular energy transfer," *Chem. Phys.*, vol. 135, pp. 195–201, 1989.

[39] S. M. Seltzer and M. J. Berger, "Evaluation of the collision stopping power of elements and compounds for electrons and positrons," *Int. J. Appl. Rad. Isot.*, vol. 33, no. 11, pp. 1189–1218, 1982.

[40] F. Rohrlich and B. C. Carlson, "Positron-electron differences in energy loss and multiple scattering," *Phys. Rev.*, vol. 93, no. 1, pp. 38–44, 1954.

[41] R. M. Sternheimer, "General expression for the density effect for the ionization loss of charged particles," *Phys. Rev. B*, vol. 24, no. 11, pp. 6288–6291, 1981.

[42] J. B. Birks, "Scintillations from organic crystals: Specific fluorescence and relative response to different radiations," *Proc. Phys. Soc. A*, vol. 64, no. 10, pp. 874–877, 1951.

[43] C. N. Chou, "The Nature of the saturation effect of fluorescent scintillators," *Phys. Rev.*, vol. 87, no. 5, pp. 904–905, 1952.

[44] G. Carles, E. Gunther, G. García, and A. G. Malonda, "Ionization quenching in LSC," *Appl. Rad. Isot.*, vol. 60, no. 2–4, pp. 447–451, 2004.

[45] R. Pereira, "Scintillator calibration for the AMS prototype test at CERN," 2004. AMS RICH meeting, Grenoble, ams.cern.ch/AMS/Analysis/rich.html.

[46] G. T. Wright, "Scintillation response of organic phosphors," *Phys. Rev.*, vol. 91, no. 5, pp. 1282–1283, 1953.

[47] H. Kallmann and G. J. Brucker, "Decay Times of Fluorescent Substances Excited by High-Energy Radiation," *Phys. Rev.*, vol. 108, no. 5, pp. 1122–1130, 1957.

[48] M.-N. Peron and P. Cassette, "Mesure de la réponse lumineuse de scintillateurs liquides à des électrons mono-énergétiques d'énergie inférieure à 100 keV," *Bulletin du BNM*, no. 105, pp. 34–44, 1996.

[49] R. Voltz, J. L. da Silva, G. Laustriat, and A. Coche, "Influence of the nature of ionizing particles on the specific luminescence of organic scintillators," *J. Chem. Phys.*, vol. 45, no. 9, pp. 3306–3311, 1966.

[50] R. Voltz, H. Dupont, and G. Laustriat, "Radioluminescence des milieux organiques. II. Vérification expérimentale de l'étude cinétique," *J. Phys. France*, vol. 29, no. 4, pp. 297–305, 1968.

[51] S. P. Ahlen, B. G. Cartwright, and G. Tarlé, "Return to unsaturated response of polymeric scintillators excited by relativistic heavy ions," *Nucl. Instr. and Meth.*, vol. 147, no. 3, pp. 321–328, 1977.

[52] O. Klein and Y. Nishina, "Über die Streuung von Strahlung durch freie Elektronen nach der neuen relativistischen Quantendynamik von Dirac," *Zeitschrift f. Physik A*, vol. 52, no. 11–12, p. 853, 1929.

[53] O. Stern and M. Volmer, "Über die Abklingungszeit der Fluoreszenz," *Physikalische Zeitschrift*, vol. 20, pp. 183–188, 1919.

[54] J. Haser, 2010. personal communication.

[55] International Commission on Radiation Units and Measurements, *Stopping Powers for Electrons and Positrons*, vol. 60 of *ICRU Report*. Bethesda, 1984.

[56] C. Aberle, 2010. personal communication.